



1           **Influence of nitrogen oxides and volatile organic compounds emission changes on**  
2                           **tropospheric ozone variability, trends and radiative effect**

3    Suvarna Fadnavis<sup>1</sup>, Yasin Elshorbany<sup>2</sup>, Jerald Ziemke<sup>3</sup>, Brice Barret<sup>4</sup>, Alexandru Rap<sup>5</sup>, PR  
4    Satheesh Chandran <sup>1</sup>, Richard J. Pope<sup>5</sup>, Vijay Sagar<sup>1</sup>, Domenico Taraborrelli<sup>6</sup>, Eric Le  
5    Flochmoe<sup>3</sup>, Juan Cuesta<sup>7</sup>, Catherine Wespes<sup>8</sup>, Folkert Boersma<sup>9,10</sup>, Isolde Glissenaar<sup>9</sup>, Isabelle  
6    De Smedt<sup>11</sup>, Michel Van Roozendael<sup>11</sup>, Hervé Petetin<sup>12</sup>, Isidora Anglou<sup>9</sup>

7  
8    <sup>1</sup>Center for Climate Change Research, Indian Institute of Tropical Meteorology, MoES, Pune,  
9    India

10   <sup>2</sup>School of Geosciences, College of Arts and Sciences, University of South Florida, St.  
11   Petersburg, FL, USA

12   <sup>3</sup>NASA Goddard Space Flight Center, Greenbelt, Maryland, USA

13   <sup>4</sup>LAERO/OMP, Université Paul Sabatier, Université de Toulouse-CNRS, Toulouse, France

14   <sup>5</sup>School of Earth and Environment, University of Leeds, Leeds, UK; National Centre for Earth  
15   Observation, University of Leeds, Leeds, UK

16   <sup>6</sup>Institute of Climate and Energy Systems, ICE-3: Troposphere, Forschungszentrum Jülich  
17   GmbH, Jülich, Germany,

18   <sup>7</sup>University Paris Est Creteil and Université Paris Cité, CNRS, LISA, F-94010 Créteil, France

19   <sup>8</sup>Université libre de Bruxelles (ULB), Spectroscopy, Quantum Chemistry and Atmospheric  
20   Remote Sensing, Brussels, Belgium

21   <sup>9</sup>Royal Netherlands Meteorological Institute (KNMI), De Bilt, The Netherlands

22   <sup>10</sup>Wageningen University, Environmental Sciences Group, Wageningen, The Netherlands

23   <sup>11</sup>Belgian Institute for Space Aeronomy, Brussels, Belgium

24   <sup>12</sup>Barcelona Supercomputing Center, Barcelona, Spain

25

26

27   **Corresponding author email: suvarna@tropmet.res.in**

28

29

30

31

32

33



34 **Abstract**

35 Ozone in the troposphere is a prominent pollutant whose production is sensitive to the  
36 emissions of nitrogen oxides (NO<sub>x</sub>) and volatile organic compounds (VOC). In this study, we  
37 assess the variation of tropospheric ozone levels, trends, ozone photochemical regimes, and  
38 radiative effects using the ECHAM6–HAMMOZ chemistry-climate model for the period 1998  
39 – 2019 and satellite measurements. The global mean simulated trend in Tropospheric Column  
40 Ozone (TRCO) during 1998 – 2019 is 0.89 ppb decade<sup>-1</sup>. The simulated global mean TRCO  
41 trends (1.58 ppb decade<sup>-1</sup>) show fair agreement with OMI/MLS (2005 – 2019) (1.4 ppb  
42 decade<sup>-1</sup>). The simulations for doubling emissions of NO<sub>x</sub> (DNO<sub>x</sub>), VOCs (DVOC), halving  
43 of emissions NO<sub>x</sub> (HNO<sub>x</sub>) and VOCs (HVOC) show nonlinear responses to ozone trends and  
44 tropospheric ozone photochemical regimes. The DNO<sub>x</sub> simulations show VOC–limited  
45 regimes over Indo-Gangetic Plains, Eastern China, Western Europe, and the eastern US, while  
46 HNO<sub>x</sub> simulations show NO<sub>x</sub>–limited regimes over America and Asia. Emissions changes in  
47 NO<sub>x</sub> (DNO<sub>x</sub>/HNO<sub>x</sub>) influence the shift in tropospheric ozone photochemical regimes  
48 compared to VOCs (DVOC/HVOC).

49

50 Further, we provide estimates of tropospheric ozone radiative effects (TO3RE). The estimated  
51 global mean TO3RE during 1998 – 2019 from the CTL simulations is 1.21 W m<sup>-2</sup>. The global  
52 mean TO3RE shows enhancement by 0.36 W m<sup>-2</sup> in DNO<sub>x</sub> simulations than CTL. While  
53 TO3RE shows reduction in other simulations compared to CTL (DVOC: by -0.005 W m<sup>-2</sup>;  
54 HNO<sub>x</sub>: by -0.12 W m<sup>-2</sup>; and HVOC: by -0.03 W m<sup>-2</sup>). The impact of anthropogenic NO<sub>x</sub>  
55 emissions is higher on TO3RE than VOCs emissions globally.

56

57 Key words: Tropospheric ozone, trends, ozone photochemical regimes; ozone radiative effect.  
58 FNR; ECHAM6-HAMMOZ model simulations.

59



## 60 1. Introduction

61 Tropospheric ozone, a major air pollutant, has been a pressing issue in recent decades  
62 due to its detrimental effect on human health and ecosystem productivity and as a short-term  
63 climate forcer (Riese et al. 2012; Gulev et al., 2021; Wang et al., 2022). Considering these  
64 harmful impacts, the assessment of tropospheric ozone levels and trends are being conducted  
65 frequently (Gaudel et al., 2018; Mills et al., 2018; Tarasick et al., 2019). Ozone trends are being  
66 assessed from surface observations, in-situ and ground-based measurements, satellite  
67 retrievals, and model simulations (Cooper et al., 2014; Cohen et al., 2018; Young et al., 2018;  
68 Tarasick et al., 2019; Archibald et al., 2020). The latest IPCC AR6 reported an enhancement  
69 in free tropospheric ozone by 2 – 7% decade<sup>-1</sup> in the northern mid-latitudes, 2 – 12% per decade  
70 in the tropics, and <5% decade<sup>-1</sup> in southern mid-latitudes (Gulev et al., 2021; Szopa et al.,  
71 2021). The Tropospheric Ozone Assessment Reports (TOAR) (Cooper et al., 2014; Lefohn et  
72 al., 2017; Schultz et al., 2017; Fleming et al., 2018; Gaudel et al., 2018; Mills et al., 2018;  
73 Young et al., 2018; Tarasick et al., 2019) have documented global increases of tropospheric  
74 column ozone (TRCO) in the 20th century. Increasing tropospheric trends are explained by  
75 enhanced anthropogenic emissions (Cooper et al., 2014; Zhang et al., 2016) and modulation by  
76 climate variability (Lin et al., 2014; Lu et al., 2018). Several studies have documented  
77 increasing trends in TRCO across various regions and different time periods.

78

79 For instance, enhancement in TRCO trends globally using measurements from multiple  
80 sources such as Global Observing System database (IAGOS) and ozonesondes and GEOS–  
81 Chem model simulation revealed increases of  $2.7 \pm 1.7$  and  $1.9 \pm 1.7$  ppb decade<sup>-1</sup> between  
82 1995 and 2017 (Wang et al., 2022). Additionally, Fiore et al. (2022) also found increasing  
83 trends ranging from 0.6 to 2.5 ppb decade<sup>-1</sup> from 1950 to 2014 globally based on IAGOS  
84 measurements and the Community Earth System, version-2, the Whole Atmosphere  
85 Community Climate Model, version-6 (CESM2–WACCM6) model study. Furthermore, trends  
86 in TRCO are stronger in the Northern Hemisphere (NH) than Southern Hemisphere (SH) due  
87 to larger anthropogenic emissions (Monks et al., 2015). Ozone Monitoring Instrument (OMI)  
88 and Microwave Limb Sounder (MLS) observations from 2005 until 2010 show annual TRCO  
89 trends averaged over the NH exceed the SH average by 4% at low latitudes (0° – 25°), by 12%  
90 at mid-latitudes (25° – 50°), and by 18% at high latitudes (50° – 60°) (Cooper et al., 2014).  
91 Recently, a decrease in TRCO trends after the Corona–Virus Disease 2019 (COVID–19)



92 outbreak has been reported by several studies, e.g., Chang et al. (2022, 2023) and Steinbrecht  
93 et al. (2021) showed a decrease in tropospheric ozone in 2020 due to the COVID–19 lockdown.  
94 Also, Putero et al. (2023) show widespread ozone decreases at high-elevation sites in 2020.  
95 However, our study period (1998–2019) excludes the COVID–19 associated emission changes.

96

97 The trends in surface ozone have grown during the last century; however, a few  
98 locations show decreasing trends (Cooper et al., 2014). The UKESM1 model simulations show  
99 that global mean surface ozone increased by ~28% throughout the twentieth century (Archibald  
100 et al., 2020). The set of lower tropospheric and surface ozone measurements in the NH shows  
101 an increase in ozone by 30%–70% since the middle of the 20th Century (Gulev et al., 2021).  
102 Recent observations from UV-absorption analyzers from 2000 – 2021 in southwestern Europe  
103 show an increase in ozone trends of  $2.2 \pm 0.3$  ppb decade<sup>-1</sup> (Adame et al., 2022). Cooper et al.  
104 (2014) reported that surface ozone trends have varied over different regions from 1990 until  
105 2010. In Western Europe, ozone concentration increased in the 1990s, followed by a levelling  
106 off or decrease since 2000. Analysis of monthly surface ozone anomaly data from 2000 to 2018  
107 shows the strongest negative trend of  $-2.8 \pm 1.1$  ppb decade<sup>-1</sup> at the Gothic station (41° N, 2.1°  
108 E) and the strongest positive trend of  $2.2 \pm 0.9$  ppb decade<sup>-1</sup> at American Samoa (14° S, 171°  
109 W) (Cooper et al., 2014). Lu et al. (2018) reported that the surface ozone trends varied between  
110 0.17 % to 0.81 % in the SH from 1990 to 2015. CMIP6 models showed that the tropospheric  
111 ozone burden increased by 44 % in 2005 – 2014 compared to 1850 (Griffiths et al., 2021).

112

113 NO<sub>x</sub> or VOC are the major precursors that define ozone photochemical regimes  
114 (Duncan et al 2010). Information on ozone photochemical regimes is of utmost importance to  
115 know ozone levels. However, the non-linearity in the O<sub>3</sub> – NO<sub>x</sub> – VOC chemistry has always  
116 posed a challenge in identifying photochemical regimes. The regime is called NO<sub>x</sub>–limited if  
117 the ozone production is directly related to a change in NO<sub>x</sub>, with no impact from VOC  
118 perturbations. Whereas the region where ozone production is regulated by the ambient  
119 availability of VOCs is called VOC–limited (Sillman et al., 1990; Kleinman, 1994). The ratios  
120 such as O<sub>3</sub>/(NO<sub>y</sub>-NO<sub>x</sub>), HCHO/NO<sub>y</sub>, HCHO/NO<sub>2</sub>, H<sub>2</sub>O<sub>2</sub>/HNO<sub>3</sub> are adopted to diagnose the  
121 ozone photochemical regimes (e.g., Sillman, 1995; Martin et al., 2004; Duncan et al., 2010).  
122 Among these, the most widely used indicator to identify regimes is the Formaldehyde (HCHO)  
123 to Nitrogen dioxide (NO<sub>2</sub>) Ratio (FNR) (Martin et al., 2004; Duncan et al., 2010). In our study,



124 we adopt FNR to identify NO<sub>x</sub>-limited or VOC-limited regimes. On par with the current effort  
125 to mitigate ozone pollution, it is important to understand how the changes in emissions of NO<sub>x</sub>  
126 and VOC affect the ozone photochemical regimes and trends (Jin et al., 2017, 2020).

127

128 Ozone is the third strongest anthropogenic greenhouse gas forcer, also called a short-  
129 lived climate forcer producing a global average radiative forcing of 0.47 [0.24 to 0.71 W m<sup>-2</sup>]  
130 [5% to 95% uncertainty range] (Forster et al., 2021). Recent studies showed ozone effective  
131 radiative forcing (ERF) of 0.51 [0.25 to 0.76] W m<sup>-2</sup> during 1750 – 2023 (Forster et al., 2024).  
132 The global mean radiative forcing of +0.35 W.m<sup>-2</sup> due to ozone during 1750 – 2011 is reported  
133 by Myhre et al. (2013). The CMIP6 model from 1850 to 2014 estimates an ozone radiative  
134 forcing of 0.39 W.m<sup>-2</sup> [0.27 to 0.51] (Skeie et al., 2020). The knowledge of ozone radiative  
135 forcing due to changes in anthropogenic emissions of NO<sub>x</sub> and VOC will help to assess climate  
136 change. Therefore, we also show the impacts of enhanced or reduced emissions of NO<sub>x</sub> and  
137 VOC on ozone radiative forcing in addition to ozone trends and photochemical regimes. To  
138 achieve this, we conducted sensitivity experiments by doubling and halving global NO<sub>x</sub> and  
139 VOC emissions using the state-of-the-art chemistry-climate model ECHAM6-HAMMOZ for  
140 the period 1998–2019. The paper is outlined as follows: satellite data and the model  
141 experimental setup are given in section 2, and results are given in section 3, which includes a  
142 comparison of simulated tropospheric column ozone with satellite data and estimated ozone  
143 trends. Discussions on ozone photochemical regimes and their trends are made in sections 4 to  
144 6. Estimates of ozone radiative effects are given in section 7. Conclusions are made in section  
145 8.

146

## 147 **2. Satellite data and model experiments**

### 148 **2.1. OMI Satellite Data.**

149 We include OMI/MLS tropospheric column ozone (TRCO) for October 2004 – December 2019  
150 and OMI NO<sub>2</sub>, HCHO data for latitude range 60° S – 60° N (Ziemke et al., 2006; De Smedt et  
151 al., 2021; Lamsal et al., 2021). OMI/MLS TRCO is determined by subtracting MLS  
152 stratospheric column ozone (SCO) from OMI total column ozone each day at each grid point.  
153 Tropopause pressure used to determine the SCO invoked the World Meteorological  
154 Organization (WMO) 2 K km<sup>-1</sup> lapse-rate definition from the NCEP reanalysis. The MLS data



155 used to obtain SCO were derived from the MLS v4.2 ozone profiles. We estimate  $1\sigma$  precision  
156 for the OMI/MLS monthly mean gridded TRCO product to be about 1.3 DU. Adjustments for  
157 drift calibration and other issues (e.g., OMI row anomaly) affecting OMI/MLS TRCO are  
158 discussed by Ziemke et al. (2019) and Gaudel et al. (2024).

159 We used OMI monthly mean Level 3 (L3) data for  $\text{NO}_2$  and HCHO  
160 (<https://doi.org/10.18758/h2v1uo6x>) that were produced in the context of the ESA CCI+  
161 precursors for aerosols and ozone project (De Smedt et al., 2021; Anglou et al., 2024). The  
162 datasets consist of the monthly mean tropospheric column densities for  $\text{NO}_2$  and HCHO (based  
163 on the QA4ECV  $\text{NO}_2$  and HCHO dataset) as measured by OMI from October 2004 to March  
164 2019, and include minimum spatial and temporal coverage thresholds (De Smedt et al., 2018).  
165 OMI has an overpass time of 13.30 local time and the retrieved column densities concern clear-  
166 sky or partially cloudy conditions.

167

## 168 2.2 IASI-SOFRID

169 The Software for a Fast Retrieval of Infrared Atmospheric Sounding Interferometer (IASI) data  
170 (SOFRID) retrieves global ozone profiles from IASI radiances (Barret et al., 2011, 2021). It is  
171 based on the RTTOV (Radiative Transfer for TOVS) operational radiative transfer model  
172 jointly developed by ECMWF, Meteo-France, UKMO and KNMI within the NWPSAF  
173 (Saunders et al., 1999; Matricardi et al., 2004). The RTTOV regression coefficients are based  
174 on line-by-line computations performed using the HITRAN2004 spectroscopic database  
175 (Rothman et al., 2005), and the land surface emissivity is computed with the RTTOV UW-  
176 IRemis module (Borbás and Ruston, 2010). The IASI-SOFRID ozone for the study period  
177 (2008 to 2019) is obtained from METOP-A (2008-2018) and METOP-B (2019).

178 We use the SOFRID version 3.5 data presented and validated in Barret et al. (2021), which  
179 uses dynamical a priori profiles from an  $\text{O}_3$  profile tropopause-based climatology according to  
180 tropopause height, month, and latitude (Sofieva et al., 2014). The use of such an a priori has  
181 largely improved the retrievals, especially in the SH where the previous version was biased.  
182 The retrievals are performed for clear-sky conditions (cloud cover fraction  $< 20\%$ ). IASI-  
183 SOFRID ozone retrievals provide independent pieces of information in the troposphere, the  
184 UTLS (300 – 150 hPa), and the stratosphere (150 – 25 hPa) (Barret et al., 2021). SOFRID  
185 TRCO absolute biases relative to ozonesondes are lower than 8 % with root mean square error



186 (RMSE) values lower than 18 % across the six 30° latitude bands (see Barret et al. (2021)).  
187 Importantly, Barret et al. (2021) have shown that relative to ozonesondes, TRCO from IASI–  
188 SOFRID display no drifts ( $<2.1\% \text{ decade}^{-1}$ ) for latitudes lower than 60°N and in the SH for  
189 latitudes larger than 30° ( $<3.7\% \text{ decade}^{-1}$ ). But significant drifts are observed in the SH tropics  
190 ( $-5.2\% \text{ decade}^{-1}$ ) and in the NH at high latitudes ( $12.8\% \text{ decade}^{-1}$ ).

191

### 192 **2.3 IASI+GOME2**

193 IASI+GOME2 is a multispectral approach to retrieve the vertical profile of ozone and its  
194 abundance in several partial columns. It is based on the synergy of IASI and GOME2 spectral  
195 measurements in the thermal infrared and ultraviolet spectral regions, respectively, which are  
196 jointly used to improve the sensitivity of the retrieval for the lowest tropospheric ozone (below  
197 3 km above sea level, see Cuesta et al., 2013). Studies over Europe and East Asia have shown  
198 particularly good capabilities for capturing near-surface ozone variability compared to surface  
199 in situ ozone measurements (Cuesta et al., 2018, 2022; Okamoto et al., 2023). TRCOs from  
200 IASI–GOME2 also show good agreement with several datasets of in-situ measurements for a  
201 four-year period in the tropics, with almost negligible biases and high correlations (Gaudel et  
202 al., 2024). This ozone product provides global coverage for low cloud fraction conditions  
203 (below 30%) for 12 km diameter pixels spaced 25 km apart (at nadir). The IASI–GOME2  
204 global dataset is publicly available through the French AERIS data center, with data from 2017  
205 to the present and covers the 90° S – 90° N latitude band. For this study, we use the monthly  
206 TRCO data between the surface and the tropopause for 2017 – 2019 for different latitude bands.  
207

### 208 **2.4 TROPOMI**

209 The TROPOspheric Monitoring Instrument (TROPOMI) is the sole payload on the Copernicus  
210 Sentinel–5 Precursor (Sentinel–5P or S5P) satellite, which provides measurements of multiple  
211 atmospheric trace species, including NO<sub>2</sub> and HCHO, at high spatial and temporal resolutions  
212 (Veefkind et al., 2012). TROPOMI has a daily global coverage with a spatial resolution of 5.5  
213 × 3.5 km<sup>2</sup> at nadir since a long-track pixel size reduction on 6 August 2019. We have used the  
214 ESA CCI+ Level–3 gridded 1° × 1° monthly tropospheric column of NO<sub>2</sub> (based on L2 v2.3.1,  
215 which applies a retrieval consistent with the most recent TROPOMI L2 version) and HCHO  
216 (<https://doi.org/10.18758/2imqez32>) (based on L2 v2.4.1, collection 3) data from May 2018 to



217 December 2019 for our study (De Smedt et al., 2021; Glissenaar et al., 2024). This dataset was  
218 created using the same methods as the ESA CCI+ OMI Level-3 datasets.

## 219 **2.5 The ECHAM6-HAMMOZ model experiments**

220 The ECHAM6.3–HAM2.3–MOZ1.0 aerosol chemistry–climate model (Schultz et al., 2018)  
221 used in the present study comprises the general circulation model ECHAM6 (Stevens et al.,  
222 2013), the tropospheric chemistry module, MOZ (Stevenson et al., 2006) and the aerosol  
223 module, Hamburg Aerosol Model (HAM) (Vignati et al., 2004). The gas phase chemistry is  
224 represented by the Jülich Atmospheric Mechanism (JAM) v002b mechanism (Schultz et al.,  
225 2018). This scheme is an update and an extension of terpenes and aromatics oxidation based  
226 on the MOZART-4 model (Emmons et al., 2010) chemical scheme. Tropospheric  
227 heterogeneous chemistry relevant to ozone is also included (Stadtler et al., 2018). MOZ uses  
228 the same chemical preprocessor as CAM-Chem (Lamarque et al., 2012) and WACCM  
229 (Kinnison et al., 2007) to generate a FORTRAN code containing the chemical solver for a  
230 specific chemical mechanism. Land surface processes are modelled with JSBACH (Reick et  
231 al., 2013). Biogenic VOC emissions are modelled with the MEGAN algorithm (Guenther et  
232 al., 2012) which has been coupled to JSBACH (Henrot et al., 2017). The lightning NO<sub>x</sub>  
233 emissions are parameterized in the ECHAM6–HAMMOZ as described by Rast et al. (2014).  
234 The lightning parameterization is the same in all the simulations. The model simulations were  
235 performed for the period 1998 to 2019 using the Atmospheric Chemistry and Climate Model  
236 Intercomparison Project (ACCMIP) (Lamarque et al., 2010; Van Vuuren et al., 2011) emission  
237 inventory. ACCMIP emission inventory includes emissions from agriculture and waste  
238 burning, forest and grassland fires, aircraft, domestic fuel use, energy generation including  
239 fossil fuel extraction, industry, ship traffic, solvent use, transportation, and waste management.  
240 The model was run at a T63 spectral resolution corresponding to about  $1.8^\circ \times 1.8^\circ$  in the  
241 horizontal dimension and 47 vertical hybrid  $\sigma - p$  levels from the surface up to 0.001 hPa. The  
242 details of model parameterizations and validation are described by (Fadnavis et al., 2019b,  
243 2019a, 2021b, 2021a, 2022, 2023). We performed five experiments: (1) control (CTL) and four  
244 emission sensitivity experiments: (2) doubling anthropogenic emission of NO<sub>x</sub> globally  
245 (DNO<sub>x</sub>), (3) reducing anthropogenic emissions of NO<sub>x</sub> by 50 % globally (HNO<sub>x</sub>), (4) doubling  
246 anthropogenic emissions of all VOCs globally (DVOC), (5) reducing anthropogenic emissions  
247 of all VOCs by 50 % globally (HVOC). We performed each experiment from 1998 to 2019  
248 after a spin-up of one year. We used the Representative Concentration Pathway (RCP) 8.5 high





249 emission scenario (Van Vuuren et al., 2011) in all model simulations. In each experiment, the  
250 monthly varying AMIP-II sea surface temperature and sea ice representative of the period  
251 1998–2019 were specified as a lower boundary condition. Anthropogenic VOC emissions  
252 included in the model are listed in the supplementary table S1.

253 TRCO is computed from the satellite data and model simulations by averaging O<sub>3</sub> amounts  
254 from the surface up to the tropopause. The partial tropospheric column is converted into a  
255 mixing ratio assuming a constant ozone mixing ratio in the troposphere. Tropopause considered  
256 is as described by the WMO thermal tropopause definition, the lowest level at which the  
257 temperature lapse rate decreases to 2 K km<sup>-1</sup> or less (WMO, 1957). The estimated tropopause  
258 in the satellite data will show differences since the tropopause is quite variable in space and  
259 time; its location will depend on the employed reanalysis (e.g., Hoffmann and Spang, 2022).  
260 The vertical resolution of the satellite and the ECHAM6-HAMMOZ also affect the estimated  
261 tropopause. For comparison of the model with satellite datasets, e.g., IASI-SOFRID,  
262 OMI/MLS, we use model and satellite data for the same period.

263

## 264 **2.6 Tropospheric ozone radiative effects**

265 The tropospheric ozone radiative effect (TO3RE) is calculated as in Pope et al. (2024). While  
266 the radiative effect calculated in ECHAM6-HAMMOZ also includes impacts of aerosols and  
267 dynamical effects, here we isolate TO3RE by using the Rap et al. (2015) tropospheric ozone  
268 radiative kernel derived from the SOCRATES offline radiative transfer model (Edwards and  
269 Slingo, 1996), including stratospheric temperature adjustments. To calculate the TO3RE, the  
270 monthly averaged ECHAM6-HAMMOZ simulated ozone field is multiplied by the offline  
271 radiative kernel (at every grid box). It is then summed from surface to the tropopause. The  
272 simulated ozone data are mapped onto the spatial resolution of the radiative kernel and then  
273 interpolated vertically onto its pressure grid. The equation for each grid box is

$$274 \text{TO3RE} = \sum_{\text{trop}_i=\text{surf}} \text{RK}_i \times \text{O}_{3i} \times \text{dp}_i / 100 \quad (1)$$

275 where TO3RE is the tropospheric ozone radiative effect (W m<sup>-2</sup>), RK is the radiative kernel  
276 (W m<sup>-2</sup> ppbv<sup>-1</sup> 100 hPa<sup>-1</sup>), O<sub>3</sub> is the simulated ozone grid box value (ppbv), dp is the pressure  
277 difference between vertical levels (hPa), and ‘i’ is the grid box index between the surface  
278 pressure level and the tropopause pressure. The tropopause pressure is identified based on the  
279 WMO lapse rate tropopause definition. Several past studies have used this approach of using



280 the SOCRATES offline radiative kernel with output from model simulations to derive the  
281 TO3RE (Rap et al., 2015; Scott et al., 2018; Rowlinson et al., 2020; Pope et al., 2024).

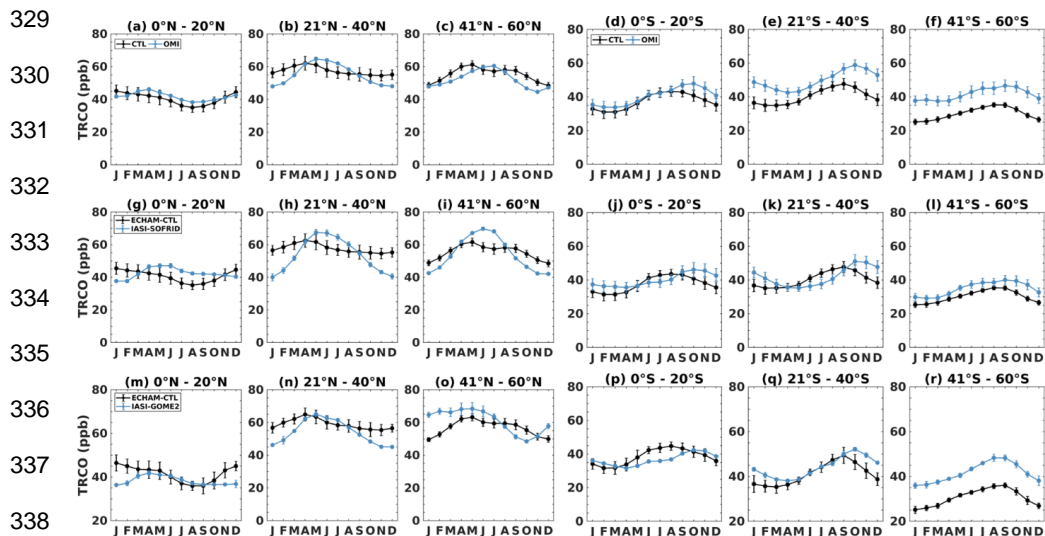
### 282 3. Results

#### 283 3.1 Comparison of the simulated seasonal cycle in TRCO, NO<sub>2</sub> and HCHO with 284 satellites retrievals

285 In this section, we compare the estimated TRCO from the model (CTL) simulation with  
286 OMI/MLS (2005 – 2019), IASI-SOFRID (2008 – 2019), and IASI-GOME2 (2017 – 2019)  
287 satellite retrievals. We compared simulated TRCO for the same period as individual satellite  
288 retrievals. The comparison of monthly mean TRCO is made for 20° latitude bins in Figure 1.  
289 In the northern tropics (0° N – 20° N) (Fig. 1a), the OMI/MLS data exhibits an annual cycle  
290 with a peak in April, whereas the model indicates a peak in January. Both datasets show a  
291 minimum in August. The model underestimates TRCO by 1.8 to 3.9 ppb during March to  
292 October. In the 21° N – 40° N and 41° N – 60° N latitude bands (Fig. 1 b–c), the model shows  
293 a one-month lead in the peak of the annual cycle compared to OMI/MLS. In the 21° N – 40°  
294 N band, the model underestimates OMI/MLS TRCO by 2.8 – 6.1 ppb during the summer  
295 months (May–August), while it overestimates TRCO by 4.1 – 8.3 ppb from October to March.  
296 The 41° N – 60° N latitude band exhibits an underestimation in the model by 1.1 – 6.3 ppb  
297 during June and July, while it overestimates (0.7 – 7.5 ppb) the rest of the year. In the Southern  
298 Hemisphere (SH), OMI/MLS and the model show a similar pattern in the seasonal cycle. The  
299 model shows a one-to-two-month lead in the annual cycle. However, the model shows an  
300 underestimation of TRCO for all months. The model underestimates TRCO by 0.5 to 7.1 ppb  
301 in the 0 – 20° S, by 5.1– 15.3 ppb in 21° S – 40° S, and by 9.2 – 13.8 ppb in the 41° S – 60° S  
302 latitude bands. The comparison of TRCO from IASI-SOFRID with the model shows features  
303 similar to those in the OMI/MLS. In the 0° N – 20° N latitude band, the model underestimates  
304 the TRCO by about 3.8 to 7.7 ppb from April to October and in the 21° N – 60° N latitude band  
305 by 1.9 – 11.3 ppb in summer (May–August). In the SH, the model shows better agreement with  
306 IASI-SOFRID than OMI/MLS. During the SH winter (June–August), the model overestimates  
307 TRCO by 2.8 – 6.5 ppb in the latitude range of 0° S – 40° S. Conversely, it underestimates  
308 TRCO by 2.7 – 8.2 ppb in the 41° S – 60° S throughout the year, which is less compared to  
309 other satellite datasets. IASI-SOFRID is known to suffer from negative drifts in the SH (Barret  
310 et al., 2021).



311 Interestingly, the model exhibits a fair agreement with IASI–GOME2 retrieved TRCO during  
312 the summer months (May–August) in the Northern Hemisphere (NH). During the winter  
313 months, the estimated TRCO shows a large overestimation of 8.3 – 11.7 ppb in the NH (0° N  
314 – 40° N), while it is underestimated by 8.3 – 11.7 ppb in the 41° N – 60° N. In the SH, a fairly  
315 good agreement is observed between the model and IASI–GOME2 TRCO, especially in the 0°  
316 S – 40° S latitude band. The model overestimates the TRCO by 7.4 – 8.8 ppb in the 0° S – 20°  
317 S during SH winter and underestimates by 4.7 – 6.7 ppb in the 21° S – 40° S belt during SH  
318 summer (December–January–February). An overall underestimation of about 7 – 11.2 ppb in  
319 TRCO is noted in the 41° S – 60° S throughout the year. Figure 1 shows that a peak in the  
320 seasonal cycle in the model is earlier than the three satellite data between 40° N and 40° S. In  
321 general, the model underestimates TRCO in summer in the NH and overestimates in winter  
322 relative to OMI/MLS, and IASI–SOFRID. In the SH, the model underestimates TRCO  
323 throughout the year compared to OMI/MLS, IASI–SOFRID, and IASI–GOME2, especially in  
324 the 41° N – 60° N band. Although the model–satellite comparison is done for the same period,  
325 the differences in sampling between the model and satellite measurements may cause the  
326 observed differences. It should be noted that the spatial resolution, coverage, and diurnal  
327 sampling time differ among the satellites which also contribute to the observed differences  
328 among them.



339 Figure 1. Time series of monthly mean TRCO (ppb) averaged for 20° wide latitude bins from  
340 (a–f) OMI/MLS (blue) and ECHAM6–HAMMOZ CTL simulations (black) for the time period



341 October 2004 – December 2019. (g–l) same as (a–f) but for IASI–SOFRID (blue) and  
342 ECHAM6–HAMMOZ CTL simulations (black) for the period January 2008 – December 2019,  
343 and (m–r) same as (a–f) but for IASI–GOME2 (blue) and ECHAM6–HAMMOZ CTL  
344 simulations (black) for the time period January 2017 – December 2019. The vertical bars in all  
345 the figures represent  $2\sigma$  standard deviation.

346

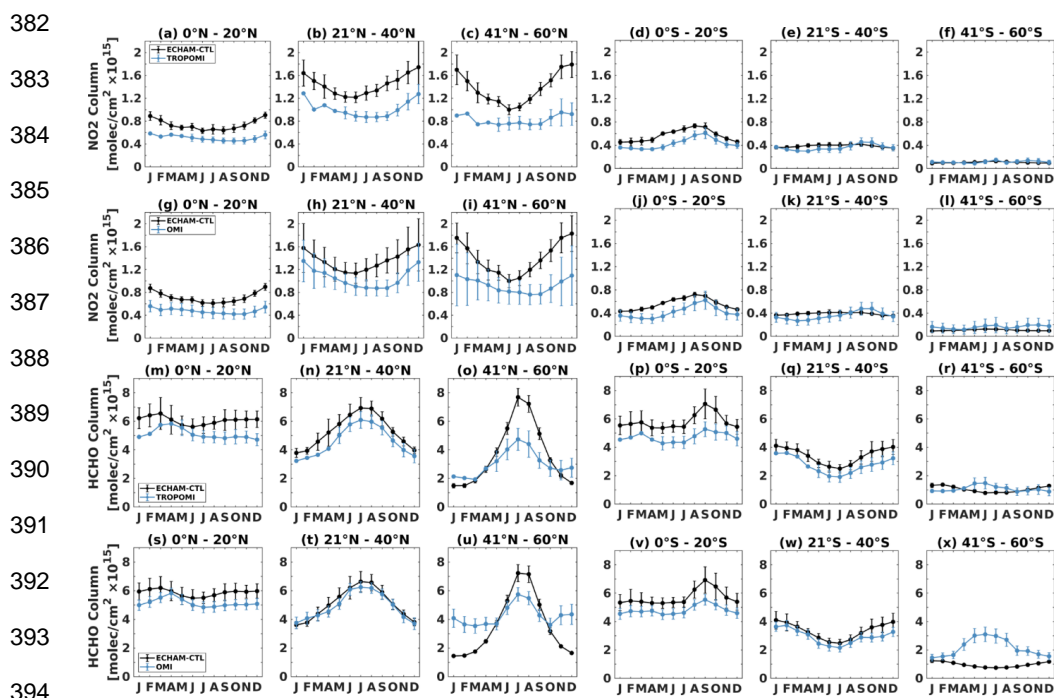
347 To evaluate our model simulations of  $\text{NO}_2$  and HCHO, we compare the simulated tropospheric  
348 column  $\text{NO}_2$  and HCHO with the ESA CCI+ monthly averaged TROPOMI and OMI data (Fig.  
349 2). The simulated  $\text{NO}_2$  reproduces the seasonal cycle but shows overestimation in the entire  
350 latitude band except  $41^\circ \text{S} - 60^\circ \text{S}$  in the SH. In the NH, the magnitude of overestimation in  
351 the simulated  $\text{NO}_2$  increases with latitude. Simulated  $\text{NO}_2$  is overestimated by 0.15 to 0.35  
352  $\times 10^{15}$  molecules  $\text{cm}^{-2}$  in  $0^\circ \text{N} - 20^\circ \text{N}$ , by 0.3 to  $0.6 \times 10^{15}$  molecules  $\text{cm}^{-2}$  in  $21^\circ \text{N} - 40^\circ \text{N}$ ,  
353 and by 0.25 to  $0.9 \times 10^{15}$  molecules  $\text{cm}^{-2}$  in  $41^\circ \text{N} - 60^\circ \text{N}$  latitude bands compared to  
354 TROPOMI. Similarly, simulated  $\text{NO}_2$  is overestimated compared to OMI by 0.16 to  $0.35 \times 10^{15}$   
355 molecules  $\text{cm}^{-2}$  in  $0^\circ \text{N} - 20^\circ \text{N}$ , by 0.16 to  $0.48 \times 10^{15}$  molecules  $\text{cm}^{-2}$  in  $21^\circ \text{N} - 40^\circ \text{N}$ , and  
356 by 0.18 to  $0.76 \times 10^{15}$  molecules  $\text{cm}^{-2}$  in  $41^\circ \text{N} - 60^\circ \text{N}$  latitude belt (Fig. 2a–c and 2g–i).  
357 Although the model overestimates  $\text{NO}_2$  in the SH, the magnitude of this overestimation is  
358 smaller compared to NH. Simulated  $\text{NO}_2$  shows a fairly good agreement from  $21^\circ \text{S}$  to  $60^\circ \text{S}$   
359 latitudes in the SH (Fig. 2d–f and 2j–l).

360

361 While the simulated HCHO successfully reproduces the seasonal cycle in both hemispheres, it  
362 shows a large overestimation, particularly in the tropical region (Fig. 2m–x). The  
363 overestimation is most pronounced when compared to TROPOMI, especially in the tropics,  
364 and to a lesser extent with OMI. The model HCHO aligns reasonably well with both TROPOMI  
365 and OMI in the northern and southern mid-latitudes ( $21^\circ \text{N} - 40^\circ \text{N}$  and  $21^\circ \text{S} - 40^\circ \text{S}$ ) with a  
366 modest overestimation of  $0.4 - 1.2 \times 10^{15}$  molecules  $\text{cm}^{-2}$  and  $0.3 - 0.5 \times 10^{15}$  molecules  $\text{cm}^{-2}$   
367 respectively in the NH and  $0.4 - 1 \times 10^{15}$  molecules  $\text{cm}^{-2}$  and  $0.5 - 1.4 \times 10^{15}$  molecules  $\text{cm}^{-2}$   
368 respectively in the SH. However, in the  $41^\circ \text{N} - 60^\circ \text{N}$  band, the model overestimates HCHO  
369 compared to TROPOMI (OMI) by  $0.6 - 2.9$  ( $0.5 - 1.7$ )  $\times 10^{15}$  molecules  $\text{cm}^{-2}$  during the NH  
370 from May to October and underestimates it by  $0.08 - 1.1$  ( $0.01 - 2.7$ )  $\times 10^{15}$  molecules  $\text{cm}^{-2}$   
371 during other months. On the contrary, the model underestimates HCHO in the  $41^\circ \text{S} - 60^\circ \text{S}$   
372 during SH winter. It should be noted that TROPOMI/OMI monthly means are valid for clear-  
373 sky situations, whereas the model simulations are all-day all-sky averages. In previous studies  
374 (Boersma et al. (2016) and references therein), it was shown that  $\text{NO}_2$  is typically 15 – 20 %



375 lower on clear-sky days than under cloudy situations due to higher photolysis rates, and faster  
 376 chemical loss of NO<sub>2</sub>. Further, OMI and TROPOMI cannot sample for snowy scenes, and  
 377 nighttime. There is significantly lower coverage on the NH during winter and vice versa for  
 378 SH. These all can likely cause model and satellite differences. For HCHO the effect is smaller  
 379 because HCHO is both produced and destroyed by OH (see Fig. 4 in Boersma et al. 2016).  
 380 Considering these differences, we proceed with the analysis of TRCO trends, ozone  
 381 photochemical regimes, and ozone radiative effects.



395 Figure 2. Time series of monthly mean tropospheric column NO<sub>2</sub> (molecules/cm<sup>2</sup>) averaged  
 396 for 20° wide latitude bins from ECHAM6–HAMMOZ CTL simulations (black) for the time  
 397 period same as (a–f) TROPOMI from May 2018 to December 2019, and (g–l) OMI from  
 398 January 2005 to December 2019. (m–x) are the same as that of (a–l) but for HCHO. The vertical  
 399 bars in the figures represent 2σ standard deviation.

400

### 401 3.2. Impacts of emission changes on the spatial distribution of ozone

402 Figure 3 shows the spatial distribution of the simulated surface (Fig. 3a–e) and TRCO (Fig. 3f–  
 403 j) concentration from ECHAM CTL simulations and the anomalies obtained from differences



404 in DNO<sub>x</sub> - CTL, DVOC - CTL, HNO<sub>x</sub> - CTL, and HVOC - CTL simulations for the period  
405 1998 – 2019. The CTL simulation shows high surface ozone levels (19 – 61.1 ppb) between  
406 10° N – 40° N (Fig. 3a). Doubling of NO<sub>x</sub> emission (DNO<sub>x</sub>) causes a global mean  
407 enhancement of surface ozone anomalies by 4.1 [-3.8 to 13], [5<sup>th</sup> to 95<sup>th</sup> percentile] ppb. Surface  
408 ozone anomalies show an increase of 5 – 20 ppb across most of the globe, excluding highly  
409 urbanized regions like the Indo-Gangetic plains (IGP), Southeast China, Northeastern United  
410 States (US), and Europe. (Fig. 3b). Over these regions, a large reduction (8 – 20 ppb) in surface  
411 ozone anomalies is noticed, indicating ozone titration by NO<sub>x</sub>. While surface ozone anomalies  
412 from DVOC - CTL simulations show global mean enhancement by 0.9 [0.1 to 2.3] ppb, its  
413 magnitude is less than that of the anomalies from DNO<sub>x</sub> - CTL (Fig. 3c). The largest increase  
414 in surface ozone anomalies for DVOC is observed over IGP, Eastern China and the Eastern US  
415 (3 – 6 ppb). Interestingly, these are the same regions where a decrease in ozone anomalies is  
416 observed in the DNO<sub>x</sub> case. The decrease (increase) in ozone anomalies with an increase in  
417 NO<sub>x</sub> (VOC) emissions indicates that these regions could be NO<sub>x</sub>-saturated or VOC-limited.  
418 Reduction of NO<sub>x</sub> emissions (HNO<sub>x</sub>-CTL) simulations show a reduction in surface ozone  
419 anomalies (global mean by -2.5 [-7.2 to -0.7] ppb) except over North-Eastern China (Fig. 3d).  
420 Earlier, Souri et al. (2017) also reported that eastern Asia has witnessed a rise in surface ozone  
421 levels despite NO<sub>x</sub> control strategies, indicating the prevalence of VOC-limited  
422 photochemistry over this region (details in section 4 to 6). However, the absence of such an  
423 increase over other VOC-limited regions points towards nonlinear ozone chemistry. While  
424 HVOC - CTL stimulation causes a reduction in surface ozone anomalies (global mean -0.4 [-  
425 1.4 to 0.05] ppb), an increase is observed in South America, some parts of the US, Australia,  
426 and the Indo-China peninsula (Fig. 3e). This increase could be due to a reduction in the radical  
427 destruction of ozone caused by aromatic hydrocarbons in low NO<sub>x</sub> conditions in these regions  
428 (Taraborrelli et al., 2021).

429

430 Further, we show the impact of emission changes on the TRCO distribution (Fig. 3f–j). The  
431 estimated global mean TRCO from the CTL simulation from 1998 to 2019 is 39.4 [23.8 to  
432 56.8] ppb (Fig. 3f). CTL simulations show higher amounts of TRCO (40.9 to 68.8 ppb) in the  
433 latitudinal band of 20° N to 40° N. These concentrations are pronounced over South and East  
434 Asia, spanning from the Mediterranean region to eastern China (Fig. 3f). TRCO anomalies  
435 from DNO<sub>x</sub> - CTL show enhancement by 11.7 [6.9 to 19.8] ppb (global mean) (Fig. 3g).



436 Between 20° N – 40° N belt, the TRCO anomalies exceeds by 6.1 – 29.3 ppb, particularly over  
437 South Asia. Interestingly, in highly urbanized areas such as the IGP, Southeast China,  
438 Northeast US, and Europe, there is only a marginal increase in TRCO anomalies (~5 ppb). This  
439 suggests the existence of a distinct ozone photochemical regime in these regions. Further  
440 exploration of this aspect will be discussed in sections 4 to 6.

441 The impact of the doubling of VOC emissions (anomalies from DVOC - CTL simulations) on  
442 TRCO is depicted in Figure 3h. An increase in global mean TRCO by 1 [-0.2 to 2.4] ppb is  
443 observed in this emission scenario. It should be noted that TRCO anomalies from DVOC -  
444 CTL are ten times less than that from DNOx - CTL (Fig. 3g and 3h). Large values of TRCO  
445 anomalies (1.5 – 2) are observed in the high latitudes (north of 60° N) and South and East Asia,  
446 with the largest values of more than 2.5 ppb over East China (e.g., Beijing). Interestingly, slight  
447 decreases in TRCO are seen in the tropical regions. This is consistent with the recent finding  
448 that aromatics, especially benzene, can lead to efficient ozone destruction in tropical UTLS  
449 (Rosanka et al., 2021). The TRCO anomalies in response to the reduction of NO<sub>x</sub> emission by  
450 50% (HNO<sub>x</sub> - CTL) show negative TRCO anomalies all over the globe (Fig. 3i). The global  
451 mean TRCO anomalies are reduced by -3.7 [-7.9 to -1.1] ppb. Large decreases in TRCO  
452 anomalies are seen over Arabia, South and East Asian regions (2.6 – 12.8 ppb). The TRCO  
453 anomalies from HVOC - CTL show an overall decrease in TRCO by -0.27 [-0.97 to -0.4] ppb  
454 (Fig. 3j). Further, a small enhancement is noted in the TRCO anomalies (by 0.5 – 1 ppb) in the  
455 southern tropics and south polar region, while a decrease of -2.3 to 0.3 ppb is observed in the  
456 NH. (Fig. 3j). Figure 3 clearly portrays that the TRCO response to NO<sub>x</sub> emission change is  
457 larger than that of VOCs. There is a spatially distinct distribution in TRCO associated with the  
458 region-specific ozone photochemical regimes (more discussion on the ozone photochemical  
459 regimes will be detailed in sections 4 – 6).

460

461

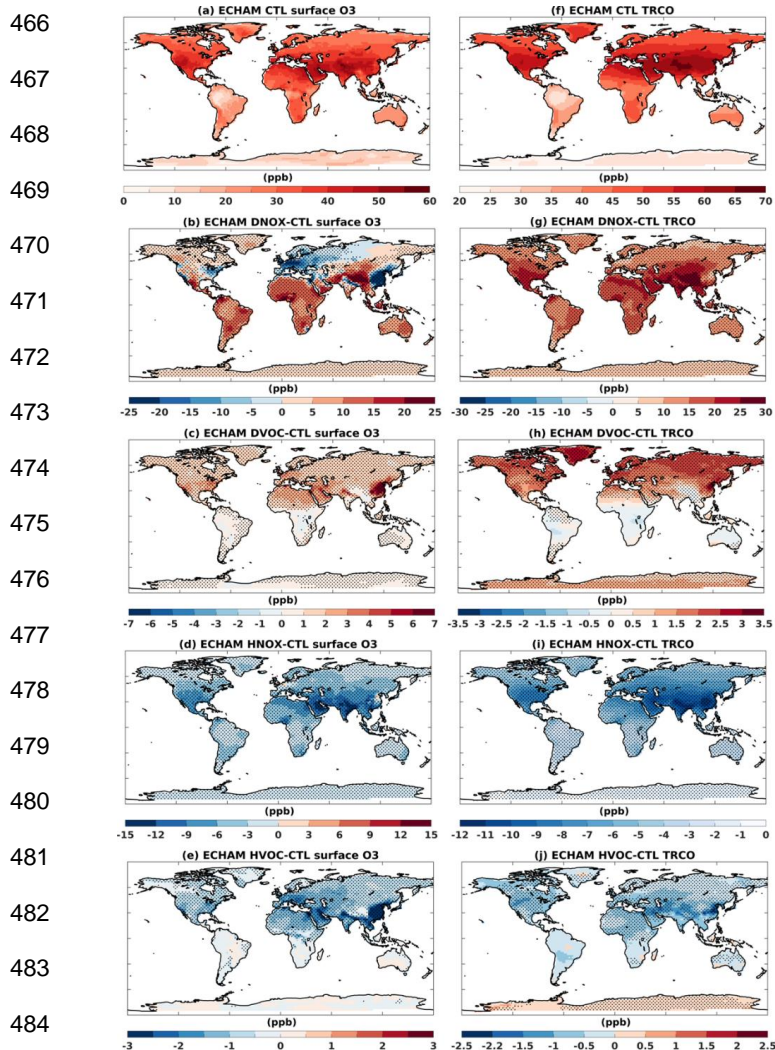
462

463

464

465





485 Figure 3. Spatial distribution of surface ozone (ppb) for (a) from CTL simulations, anomalies  
486 from (b) DNO<sub>x</sub> - CTL, (c) DVOC - CTL, (d) HNO<sub>x</sub> - CTL, and (e) HVOC - CTL simulations.  
487 (f–j) are the same as that of (a–e) but for TRCO. The stippled regions in the figures indicate  
488 anomalies significant at 95% confidence based on the t-test.

489

### 490 3.3. Spatial distribution of trends in ozone

491 We estimate trends in TRCO from ECHAM CTL simulations (1998–2019) and OMI/MLS  
492 satellite retrievals (2005–2019). The simulated trends are compared with satellite retrievals for  
493 the period 2005–2019. Since IASI–GOME2 has a short observation period (2017–2019) and





494 IASI–SOFRID has negative drift in the SH, only TRCO from OMI/MLS is considered for trend  
495 estimation (Fig. 4). The spatial pattern of trends from OMI/MLS shows fair agreement with  
496 model simulations (Fig 4a-b). Quantitatively, the global mean TRCO trend from OMI/MLS is  
497 slightly lower than the model (OMI/MLS:1.43 [-0.5 to 3.2] ppb decade<sup>-1</sup>; ECHAM-CTL: 1.58  
498 [0.3 to 3.3] ppb decade<sup>-1</sup>). Both datasets reveal high trends, ranging from 3–4 ppb decade<sup>-1</sup>,  
499 across regions such as South Asia, East Asia, and the West Pacific. OMI/MLS show negative  
500 trends over parts of Africa, South America, Australia, and the southeastern Pacific (Fig. 4b),  
501 which is not simulated in ECHAM6–HAMMOZ. Although there is fair agreement in spatial  
502 patterns of TRCO trends between OMI/MLS and the model, the minor differences may be due  
503 to the model's tendency to underestimate ozone levels and differences in the seasonal cycle. (See  
504 Fig. 1).

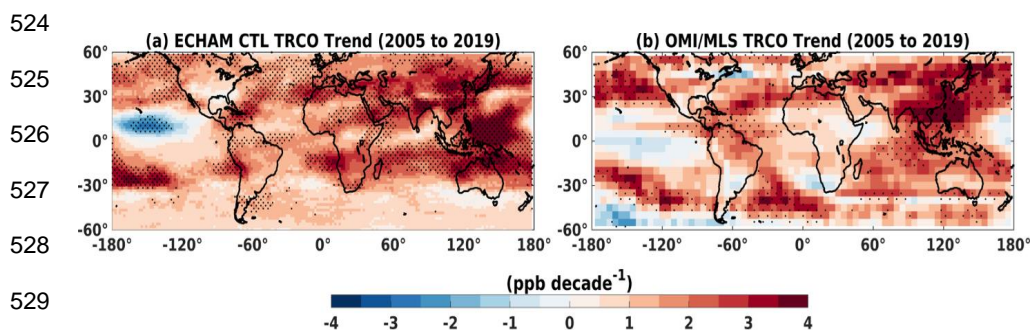
505

506 TRCO trends analyzed from the Total Ozone Mapping Spectrometer (TOMS) indicate a  
507 consistent absence of trend over the tropical Pacific Ocean, with notable positive trends (4 – 5%  
508 decade<sup>-1</sup>) seen in the mid-latitude Pacific regions of both hemispheres (Ziemke et al., 2005).  
509 This pattern is consistent across the ECHAM6–HAMMOZ and OMI/MLS data, although their  
510 magnitude differs (Fig. 4 a–b). TOMS data also showed trends of ~2 – 5% decade<sup>-1</sup> across broad  
511 regions of the tropical South Atlantic, India, Southeast Asia, Indonesia, and the  
512 tropical/subtropical regions of China during 1979 – 2003 (Ziemke et al., 2005; Beig and Singh,  
513 2007) which are also simulated in the model. Further, a large positive trend of ~2.5 ppb decade<sup>-1</sup>  
514 observed near 50° S in OMI/MLS is not simulated by the model (Fig. 4a–b). The CESM2–  
515 WACCAM6 simulation from 1950 to 2014 also shows the largest trend estimate of 0.8 Tg  
516 decade<sup>-1</sup> over 20° N – 30° N (Fiore et al., 2022). Large TRCO trends over 20° N – 30° N are  
517 also seen in OMI/MLS and the model (Fig.4). Wang et al. (2021) reported TRCO trends varying  
518 between 2.55 to 5.53 ppb decade<sup>-1</sup> during 1955–2017 over South and East Asia using IAGOS,  
519 ozonesonde observations, and Goddard Earth Observing System–chemistry model (GEOS–  
520 Chem). Our model also shows similar increasing trends.

521

522

523



531 Figure 4. Trend of TRCO (ppb decade<sup>-1</sup>) from (a) ECHAM CTL, and (b) OMI/MLS satellite  
532 for the period January 2005 to December 2020. Stippled regions in the figures indicate trends  
533 significant at 95% confidence based on the t-test.

534

535 Figure 5 shows the spatial distribution of estimated trends in surface ozone and TRCO  
536 from CTL simulation for the period 1998 – 2019. Changes (Doubling/halving) in the emission  
537 of NO<sub>x</sub> and VOCs will change ozone trends. Hence, we analyze anomalies in ozone from  
538 DNO<sub>x</sub> - CTL, DVOC - CTL, HNO<sub>x</sub> - CTL, and HVOC - CTL. The surface ozone trend in the  
539 CTL simulation shows spatial variation with a pronounced increasing trend over South Asia  
540 and the Middle East (3 – 4 ppb decade<sup>-1</sup>) (Fig. 5a). Similar pronounced increase is also seen in  
541 the TRCO trend (Fig. 5b). The estimated global mean TRCO trend from CTL is 0.89 [-0.07 to  
542 2.1] ppb decade<sup>-1</sup>. However, the negative trends in surface ozone over Mexico, certain parts of  
543 the US, and East China are barely discernible in the TRCO data. This discrepancy may stem  
544 from the interplay of mixing and transport processes, stratospheric intrusions, which are crucial  
545 when assessing ozone levels across the tropospheric column. The stratospheric ozone  
546 intrusions lead enhancement in the tropospheric ozone (Prather and Zhu, 2024).

547

548 Figure 5 c–d shows anomalies from DNO<sub>x</sub> – CTL simulations in the surface ozone and  
549 TRCO. A striking feature is large negative trend anomalies over India and China at the surface  
550 (-4.8 to -8 ppb decade<sup>-1</sup>) and TRCO (-2 to -4 ppb decade<sup>-1</sup>). Whereas Europe, the US, some  
551 parts of Africa and South America show positive trends at the surface (1.8 to 8 ppb decade<sup>-1</sup>)  
552 and TRCO (2 to 4 8 ppb decade<sup>-1</sup>). The global mean anomalies of the TRCO trend are 1.2 [-  
553 0.1 to 2.7] ppb decade<sup>-1</sup>. The high TRCO trends (1 - 3 ppb decade<sup>-1</sup>) in the North of 60° N are  
554 seen in for all the sensitivity simulations. This may be due to transport and stratospheric



555 intrusion in response to emission perturbation that affects the radiative forcing and dynamics  
556 (e.g., Fig. 5d, f, h, j).

557

558           When global emissions of VOCs are doubled, anomalies (DVOC - CTL) in trends show  
559 a decrease (by -0.8 to -1.9 ppb decade<sup>-1</sup>) in surface ozone over Europe, Africa and some parts  
560 of the US, while strong positive trend anomalies (1.6 to 2 ppb decade<sup>-1</sup>) are seen over India  
561 and China (Fig. 5e). Anomalies in TRCO trends show an enhancement over South Asia,  
562 Southwest Asia, China, parts of the Indian Ocean, and the western Pacific (0.8 to 1.6 ppb  
563 decade<sup>-1</sup>) (Fig. 5f). A global mean TRCO trend anomaly for DVOC-CTL simulation is 0.5 [-  
564 0.03 to 1.04] ppb decade<sup>-1</sup>. The estimated enhancement in global mean TRCO trend anomalies  
565 for DVOC is less than DNOx simulations. Figures 5 c and e also give indications of the  
566 existence of distinct ozone photochemical regimes globally. The increasing (decreasing) trend  
567 in surface ozone with an increase in VOC (NOx) over India and China indicates that these  
568 regions are in a VOC-limited regime, and vice-versa over the US and Europe indicates that  
569 these regions are in a NOx-limited regime (more discussions on sections 4 to 6).

570

571           Figure 5g-h shows the trend in surface and TRCO ozone anomalies from HNOx - CTL.  
572 The surface ozone trend shows a large negative trend over Europe and South Asia, while a  
573 positive trend over the US, China, and Australia (Fig. 5g). Trends in TRCO also show a large  
574 negative trend over South Asia (Fig. 5h). The ozone trends are positive over large region  
575 globally although anthropogenic NOx emissions are halved than CTL. Our investigations  
576 reveal that the trend from anomalies of VOCs in the HNOx-CTL simulations is positive over  
577 the US, India, and Europe, while negative over China. Similarly, the trend from anomalies of  
578 NOx in the HNOx-CTL simulations is positive over the US and Europe while negative over  
579 India and China (Fig. S1a-b). The strong positive trend in both VOC and NOx might have  
580 resulted in the observed positive trend in surface ozone over the US, while the strong positive  
581 trend in NOx compared to that of VOCs over Europe might have resulted in more NOx titration  
582 effect causing the observed negative trend in ozone. China, being a VOC-limited regime, the  
583 reduction in NOx can decrease the NOx titration, resulting in positive ozone trends. Over India,  
584 the positive VOC trend with a negative trend in NOx may enhance the radical destruction of  
585 ozone caused by aromatic hydrocarbons in low NOx conditions (Taraborrelli et al., 2021),



586 resulting in a negative ozone trend. Thus, for HNO<sub>x</sub> – CTL, the global mean trend anomaly is  
587 positive 0.47 [-0.76 to 1.3] ppb decade<sup>-1</sup>.

588

589 The trend in surface and TRCO ozone anomalies from HVOC – CTL is shown in Figure  
590 5i-j. A large negative trend in surface ozone is noted over IGP and China, while an insignificant  
591 positive trend is noted over the US and Europe (Fig. 5i). The TRCO trend anomalies are  
592 positive over large regions in the world with pronounced high over the mid- and high latitudes  
593 although emissions of all anthropogenic VOCs are halved (Fig. 5j). The global mean trend  
594 anomaly for HVOC - CTL is 0.37 [-0.35 to 1.02] ppb decade<sup>-1</sup>. Our analysis shows that the  
595 trend in NO<sub>x</sub> anomalies and VOC anomalies from HVOC - CTL is decreasing over both India  
596 and China (Fig S1c-d). The negative trend in precursors might have resulted in a negative trend  
597 in ozone over these regions. The absence of strong trends in TRCO (Fig. b, d, f, h, j) similar to  
598 that at the surface (Fig. a, c, e, g, i) in all the simulations indicates the potential contribution of  
599 transport in the troposphere and stratospheric intrusions in TRCO. Ozone injection through  
600 stratosphere–troposphere exchange is important source of tropospheric ozone (Prather and  
601 Zhu, 2024).

602

603

604

605

606

607

608

609

610

611

612

613

614

615

616

617



618

619

620

621

622

623

624

625

626

627

628

629

630

631

632

633

634

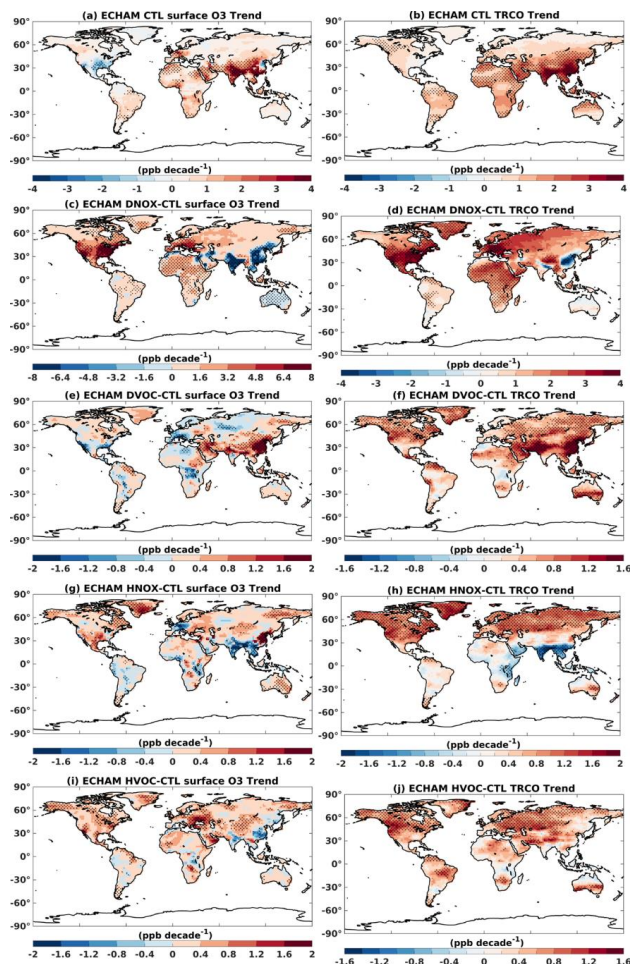
635

636

637

638

639



640 Figure 5. Trend in surface ozone (ppb decade<sup>-1</sup>) for the period 1998-2019 from (a) CTL, (c)  
641 DNOx - CTL, (e) DVOC - CTL, (g) HNOx - CTL, and (i) HVOC - CTL simulation. (b, d, f, h,  
642 and j) are the same as that of the top row but for the TRCO trend. The stippled regions in the  
643 figures indicate significance at 95% confidence based on the t-test.

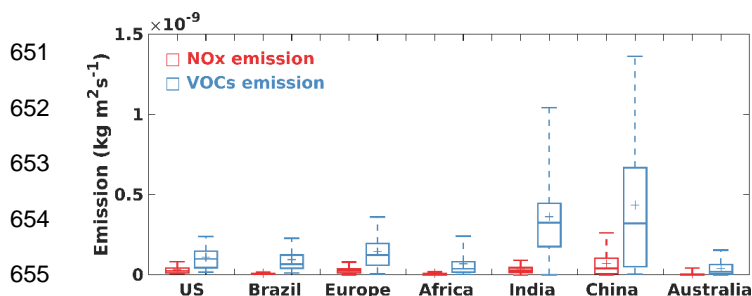
644

### 645 3.4. Trends in emission and tropospheric column of NO<sub>2</sub> and HCHO

646 We show mean emissions of NO<sub>x</sub> (NO+NO<sub>2</sub>) and HCHO over urban/semi-urban regions; US,  
647 Brazil, Europe, Africa, India, China, and Australia in Figure 6. High emissions of VOCs and  
648 NO<sub>x</sub> in India and China are evident in Figure 6. Furthermore, VOCs emissions are noted to be



649 higher than NO<sub>x</sub> over all the regions. They are higher by a factor of 3.3 in the US, 11.3 in Brazil,  
 650 4.8 in Europe, 10.5 in Africa, 10.8 in India, 6.1 in China, and 6.7 in Australia.



656 Figure 6. Box and whisker plot illustrating the NO<sub>x</sub> (NO+NO<sub>2</sub>) and VOCs emission over the  
 657 regions US (85°W – 110°W, 35°N – 44°N), Brazil (34°W – 49°W, 24°S – 3°S), European  
 658 Union (9°W – 45°E, 35°N – 55°N), Central Africa (14°W – 45°E, 0° – 14°N), India (75°E –  
 659 90°E, 8°N – 30°N), China (110°E – 125°E, 30°N – 42°N), and South Australia (134°E – 154°E,  
 660 38°S – 28°S). The box represents the 25 and 75 percentiles, and the whisker represents the 5  
 661 and 95 percentiles. The plus marker represents the mean, and the horizontal bar represents the  
 662 1 and 99 percentiles.

663

664 The trends in ozone are partly modulated by the change in the emission of its precursors and  
 665 partly by meteorology (e.g., Verstraeten et al., 2015). We show trends in emissions and  
 666 tropospheric column amounts of ozone precursors NO<sub>2</sub> and HCHO from ECHAM CTL and  
 667 OMI satellite retrievals in Figure 7. NO<sub>2</sub> and HCHO are considered here because column  
 668 densities of these will be used to identify the ozone photochemical regimes discussed later in  
 669 Sections 4–6. Emissions and tropospheric columns of HCHO and NO<sub>2</sub> from ECHAM–CTL  
 670 show large positive trends over the South and East Asian regions (Fig. 7a–d). These regions  
 671 show large positive ozone trends in both model and OMI satellite data (see Fig. 4 and 5). Over  
 672 Europe and the US, the emission trend in both HCHO and NO<sub>2</sub> from the model is negative  
 673 (Fig. 7a, c). Though a similar negative trend in tropospheric column NO<sub>2</sub> is seen over these  
 674 regions, a marginal positive trend is noted for HCHO (Fig. 7b, d). The positive trend in column  
 675 HCHO could be due to secondary production pathways from biogenic emissions or methane  
 676 oxidation and transport (e.g., Anderson et al., 2017; Alvarado et al., 2020). The positive trend  
 677 in ozone (Fig. 4a–b and 5a, f) along with a negative trend in NO<sub>2</sub> and HCHO (Fig. 7a–d) over  
 678 Europe indicates that ozone production over this region has been initially controlled by VOCs  
 679 (i.e., VOC–limited regime; detailed discussed in section 4). However, a large decreasing trend  
 680 in NO<sub>2</sub> compared to that of HCHO over this region might have decreased the NO<sub>x</sub> titration



681 effect, resulting in an increase in ozone. On the contrary, a negative trend in surface ozone (Fig.  
682 5a) along with negative trends in NO<sub>2</sub> and HCHO are seen over the US (Fig. 7a–b). The  
683 decrease in both NO<sub>2</sub> and HCHO would have resulted in a decreasing trend in surface ozone  
684 over this region. This also indicates that the US might have been in a NO<sub>x</sub>–sensitive regime  
685 before and the large negative trend in NO<sub>2</sub> might have resulted in the decreasing trend in ozone  
686 (discussed further in section 4-6).

687

688 Further we compared the simulated trends in column HCHO and NO<sub>2</sub> with the OMI retrievals  
689 for the period 2005–2019 (Fig. 7e–h). OMI shows a positive trend in tropospheric column  
690 HCHO over South Asia ( $1 - 1.5 \times 10^{15}$  molecules cm<sup>-2</sup> decade<sup>-1</sup>), parts of western China ( $0.75$   
691  $- 1.25 \times 10^{15}$  molecules cm<sup>-2</sup> decade<sup>-1</sup>), the Iranian Plateau ( $0.5 - 1 \times 10^{15}$  molecules cm<sup>-2</sup>  
692 decade<sup>-1</sup>), the Amazon ( $1 - 1.5 \times 10^{15}$  molecules cm<sup>-2</sup> decade<sup>-1</sup>), North America ( $0.5 - 1.5$   
693  $\times 10^{15}$  molecules cm<sup>-2</sup> decade<sup>-1</sup>), Europe ( $0.5 - 1 \times 10^{15}$  molecules cm<sup>-2</sup> decade<sup>-1</sup>), and central  
694 Africa ( $1 - 1.5 \times 10^{15}$  molecules cm<sup>-2</sup> decade<sup>-1</sup>). The model simulated trends show reasonable  
695 agreement with OMI, except for western areas in central Africa, north Africa, southwest and  
696 southeast China, and some parts of Australia. Over these regions OMI indicates a negative  
697 trend, while the model suggests a marginal positive trend. OMI and ECHAM CTL show a good  
698 agreement in the tropospheric column NO<sub>2</sub> trend. Both datasets show negative trends over the  
699 eastern US and Europe, and positive trends over the Middle East, and South Asia. However,  
700 differences are seen in eastern China and central Africa, where OMI indicates a negative trend,  
701 while the model shows a strong positive trend. The differences between simulated and OMI  
702 HCHO and NO<sub>2</sub> column trends may be due to sampling time and differences in seasonal cycle.  
703 Figures 4, 5, and 7 clearly indicate the impact of ozone precursors on the spatial distribution of  
704 ozone trends. This warrants a detailed discussion on the spatial distribution of ozone precursors  
705 and their impact on ozone production-sensitive regimes, which will be presented in the next  
706 section.

707

708

709

710

711

712

713

714

715





716

717

718

719

720

721

722

723

724

725

726

727

728

729

730

731

732

733

734

735

736

737

738

739

740

741

742

743

744

745

746

747

748

749

750

751

752

753

754

755

756

757

758

759

760

761

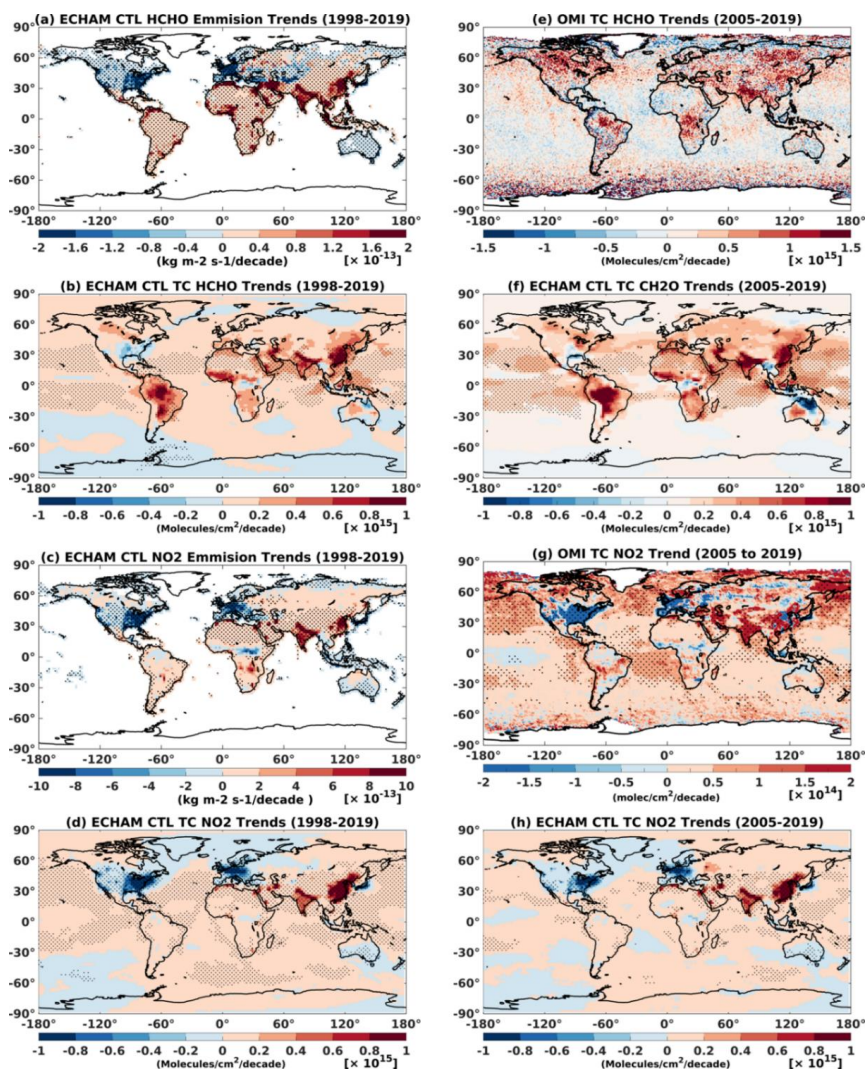


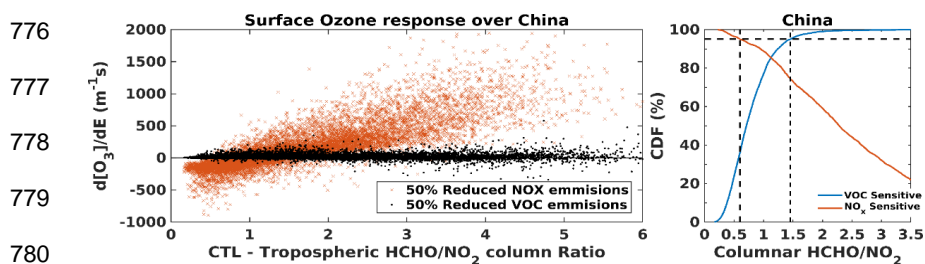
Figure 7. Trend in anthropogenic emission ( $\text{kg m}^2 \text{s}^{-1} \text{decade}^{-1}$ ) from ECHAM CTL simulation for the period 1998–2019 for (a–b) HCHO and  $\text{NO}_2$  respectively. Trends in tropospheric column (TC) ( $\text{molecules cm}^{-2} \text{decade}^{-1}$ ) for (c–d) HCHO and  $\text{NO}_2$  respectively. Trend in tropospheric column of HCHO from (e) OMI, and (f) ECHAM–CTL simulations for the period 2005–2019. (g–h) are the same as that of (e–f) but for tropospheric column  $\text{NO}_2$ . The stippled regions in the figures indicate significance at 95% confidence based on the t–test.





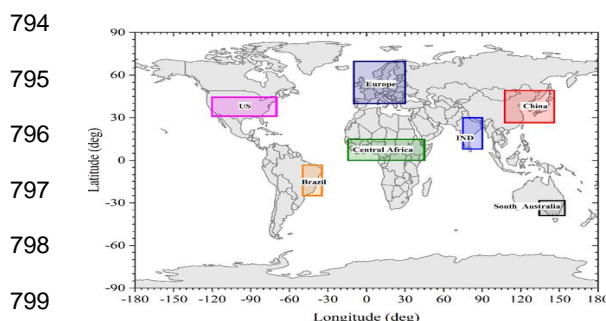
#### 762 4. Influence of NO<sub>x</sub> and VOCs emissions on Formaldehyde to Nitrogen dioxide Ratio

763 In this section, we diagnosed the spatial distribution of tropospheric ozone production  
764 sensitivity regimes (NO<sub>x</sub>-limited/VOC-limited) associated with simulations of emission  
765 changes by using formaldehyde to nitrogen dioxide ratio (FNR). We estimate the FNR  
766 thresholds from ECHAM6-HAMMOZ model simulations adhering to the methodology  
767 outlined by Jin et al. (2017). The procedure to obtain FNR involves two steps: (1) obtaining  
768 the ozone response from emission sensitivity simulations (here, HNO<sub>x</sub> and HVOC simulations)  
769 by considering only the polluted cells over the study region and plotting it as a function of FNR  
770 (Fig. 8a), (2) calculating cumulative probability from this data for the conditions  $d[\text{O}_3]/dE_{\text{NO}_x}$   
771  $< 0$  (NO<sub>x</sub> limited) and  $(d[\text{O}_3]/dE_{\text{NO}_x} > d[\text{O}_3]/dE_{\text{VOC}} > 0)$  (VOC-limited) (Fig. 8b), where  
772  $d[\text{O}_3]/dE$  represents the change in ozone corresponding to a change in emission of either NO<sub>x</sub>  
773 or VOCs. This approach is applied to estimate FNR thresholds to distinctly delineate the ozone  
774 photochemical regimes as NO<sub>x</sub> or VOC-limited over major urban and semi-urban regions. The  
775 regions considered for estimating the FNR are shown in Figure 9.



781 Figure 8. (a) Typical example of a normalized surface ozone sensitivity to a 50% reduction in  
782 global NO<sub>x</sub> (HNO<sub>x</sub>) and VOC (HVOC) emissions versus tropospheric column HCHO/NO<sub>2</sub>  
783 ratio derived from ECHAM6-HAMMOZ model simulation over China for the period 1998 –  
784 2019, (b) Cumulative probability (CP) of VOC-sensitive ( $d[\text{O}_3]/dE_{\text{NO}_x} < 0$ ) and NO<sub>x</sub>-sensitive  
785 ( $d[\text{O}_3]/dE_{\text{NO}_x} > d[\text{O}_3]/dE_{\text{VOC}} > 0$ ) conditions, as a function of tropospheric column HCHO/NO<sub>2</sub>  
786 as simulated by the ECHAM6-HAMMOZ model. The horizontal dashed line represents the  
787 95% CP, and the vertical dashed lines represent the HCHO/NO<sub>2</sub> ratio corresponding to 95%  
788 CP for both the VOC-sensitive and NO<sub>x</sub>-sensitive curves demarcating the VOC-sensitive,  
789 NO<sub>x</sub>-sensitive, and transition regimes.

790  
791  
792  
793



794  
 795  
 796  
 797  
 798  
 799  
 800 Figure 9. The rectangular box marks indicate the regions considered for estimating the  
 801 HCHO/NO<sub>2</sub> ratio (FNR).

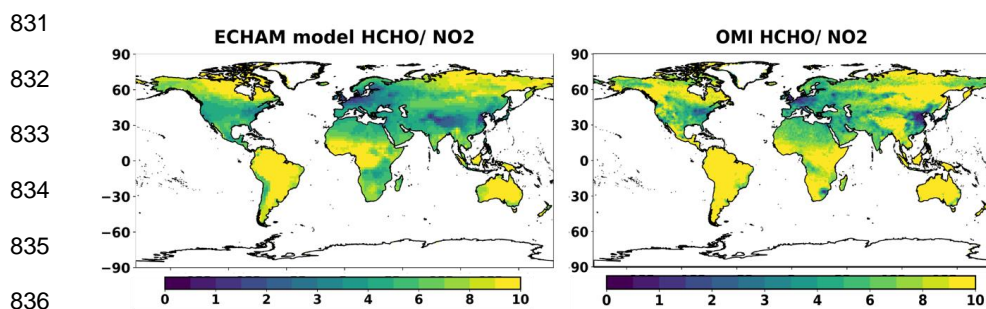
802 Table 3 presents FNR thresholds across the regions outlined in Figure 9. Based on ECHAM6–  
 803 HAMMOZ simulations, our analysis closely mirrors the threshold ranges documented in prior  
 804 research. For instance, during summer in the USA, many studies report FNR thresholds within  
 805 the 0.8 – 2 range (Chang et al., 2016; Jin et al., 2017; Roberts et al., 2022), while our  
 806 simulations indicate a range of 0.3 to 1.05. Similarly, across China, previous studies have  
 807 reported FNR thresholds spanning 1 – 2 (Lee et al., 2022) and 0.6 – 3 (Chen et al., 2023),  
 808 aligning closely with our simulated range of 0.6 – 1.45. It is interesting to note that the transition  
 809 region exhibits a very narrower range in the US, Europe, and China, indicating that the  
 810 transition from VOC–limited to NO<sub>x</sub>–limited can happen suddenly in response to changes in  
 811 the emission of NO<sub>x</sub>/VOC. Whereas the transition region is wider in Central Africa.

812 Table 3. Estimated values of the tropospheric HCHO/NO<sub>2</sub> columns threshold ratios from  
 813 ECHAM6–HAMMOZ model control simulation to identify the NO<sub>x</sub> and VOC sensitive  
 814 regimes across various regions. The FNR less than the lower limit indicates VOC–limited, and  
 815 that higher than the upper limit indicates NO<sub>x</sub>–limited regimes.

816	Sr. No.	Regions	Transition limits	
817	1	US (85° W – 110° W, 35° N– 44° N)	0.44	1.14
818	2	Brazil (34° W – 49° W, 24° S – 3° S)	3.04	7.53
819	3	European Union (9° W – 45° E, 35° N – 55° N)	0.3	1.37
820	4	Central Africa (14° W – 45° E, 0° – 14° N)	3.24	7.19
821	5	India (75° E – 90° E, 8° N – 30° N)	2.27	4.63
821	6	China (110° E – 125° E, 30° N – 42° N)	1.14	1.91
821	7	South Australia (134° E – 154° E, 38° S – 28° S)	1.03	3.28



822 Further, we compared the model-estimated FNR with the OMI-derived FNR for the period  
823 2005 – 2019. Figure 10 illustrates the comparison of FNR estimated from ECHAM6–  
824 HAMMOZ CTL simulations with OMI. The spatial map of FNR shows fairly good agreement  
825 between OMI and the model. Over the urbanized regions (e.g., South Asia, Europe, the US,  
826 and China) both the model and OMI show FNR < 4. In contrast, regions like North Canada,  
827 South America, central Africa, Australia, and Siberia exhibit high FNR values >9. There is  
828 good agreement between the model simulations and OMI, however, some minor differences  
829 are seen between the model and OMI FNR over the west coast of South America, South Africa,  
830 the Tibetan Plateau, and western Australia.



837 Figure 10. Spatial distribution of mean tropospheric column HCHO/NO<sub>2</sub> (FNR) obtained from  
838 ECHAM6–HAMMOZ CTL simulations (2005 – 2019) and OMI (2005 – 2019).

839

840 These differences could be due to the underestimation of HCHO in the model over these  
841 regions. Considering the fair performance of the model in comparison with OMI, we further  
842 analyzed the influence of changes in NO<sub>x</sub> and VOC emissions on the FNR from the model  
843 simulations, which are discussed in the subsequent sections.

844

845 Figure 11 shows the spatial distribution of FNRs estimated from CTL, DNO<sub>x</sub>, DVOC,  
846 HNO<sub>x</sub>, and HVOC simulations. In the control simulation for the period 1998 – 2019, most of  
847 the polluted cities/industrialized areas in the US, Canada, Europe, west Russia, East China,  
848 Korea and Japan are VOC limited (FNRs <2). The NO<sub>x</sub>–limited regimes (largest FNR values  
849 >5) are found over the rural or unpolluted background regions like tropical rainforest, savanna,  
850 and arid climates where biogenic emissions of VOCs are high (e.g., Millet et al., 2008; Shen et  
851 al., 2019) (see Table 3 and central Africa in Fig. 11f). The DNO<sub>x</sub> simulation yields a shift in



852 the spatial extent of VOC-limited regimes (Fig. 11b). Regions across the NH exhibit VOC-  
853 limited regimes, except central Africa, Amazonia, and north Australia. Notably, the SH exhibits  
854 minimal change in the spatial extent of VOC-limited regimes with consistent occurrences over  
855 the western coastlines of South America, Argentina, Brazil, South Africa, and southern  
856 Australia.

857

858 The DVOC simulations show (Fig. 11c) a persistent occurrence of VOC-limited regimes over  
859 Western Europe (e.g., the UK). The moderate FNR values (1 – 6) prevail across most of the  
860 NH, indicating a transition or NO<sub>x</sub>-limited regime. The spatial distribution of FNR in the SH  
861 is similar to that of the control simulation. In Figure 3b–c, the increase in ozone in response to  
862 a decrease in NO<sub>x</sub> and an increase in VOC is attributed to the existence of a VOC-limited  
863 regime over these regions. The IGP, Eastern China and the eastern US clearly indicate the  
864 VOC-limited condition. The comparison of CTL and HNO<sub>x</sub> simulation (Fig. 11d) shows the  
865 transition from VOC-limited regimes to NO<sub>x</sub>-limited regimes occurring globally.

866 The FNR distribution for HVOC simulations is similar to CTL (as depicted in Fig. 11e) without  
867 any notable change in the spatial pattern. This suggests that ozone photochemistry exhibits less  
868 sensitivity to halved VOC emissions. Figure 11 clearly depicts that DNO<sub>x</sub> and HNO<sub>x</sub>  
869 simulations greatly impact the shift in ozone photochemical regimes compared with DVOC  
870 and HVOC simulations. This indicates that ozone photochemistry is highly sensitive to changes  
871 in NO<sub>x</sub> emissions globally.

872

873

874

875

876

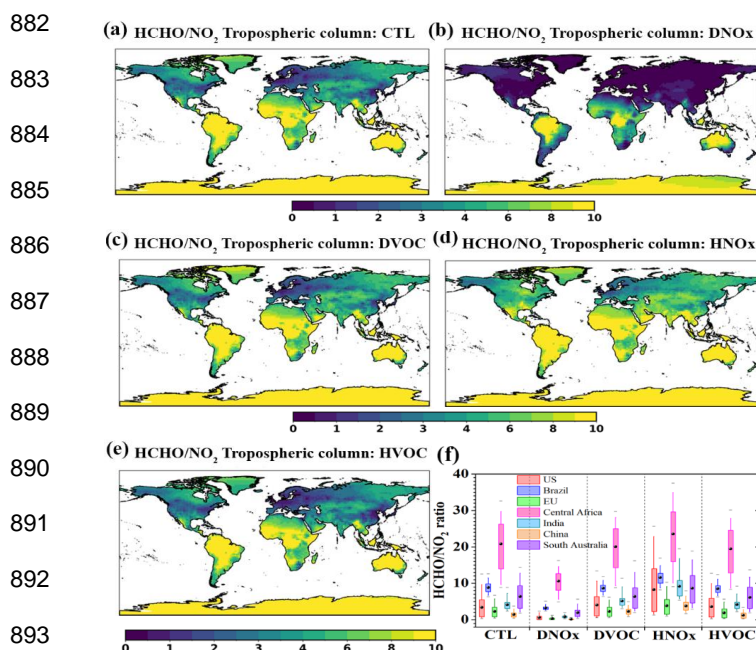
877

878

879

880

881



894 Figure 11. Spatial distribution of monthly mean tropospheric column HCHO/NO<sub>2</sub> (FNR)  
895 obtained from ECHAM6–HAMMOZ simulations (1998 – 2019) for (a) CTL, (b) DNOx, (c)  
896 DVOC, (d) HNOx, and (e) HVOC simulations. (f) Box and whisker plot illustrating the long-  
897 term average FNR over the regions depicted in Fig. 9. Box represents 25 and 75 percentile and  
898 whisker represents 5 and 95 percentiles. The black spherical marker represents the mean and  
899 the horizontal bar represents the 1 and 99 percentiles.

900

## 901 5. Seasonal variation of Formaldehyde to Nitrogen dioxide Ratio

902 Since the emission of HCHO and NO<sub>2</sub> varies with the seasons across the globe (e.g., De Smedt  
903 et al., 2015; Wang et al., 2017; Surl et al., 2018; Kumar et al., 2020; Goldberg et al., 2021;  
904 Guan et al., 2021), understanding the seasonal changes in FNR is also crucial for  
905 comprehending shifts in ozone photochemical regimes. In this regard, using the methodology  
906 described in Section 4, we extracted the seasonal changes in transition limits for the major  
907 urban and semi-urban regions shown in Figure 9 and summarized in Table 4. Figure 12  
908 illustrates the seasonal variation of estimated FNR from both OMI data and model simulations  
909 across these key urban regions. In general, all regions exhibit distinct seasonal variations in  
910 transition limits (Table 4). Previously reported transition limits over the US (2 – 5: Johnson et  
911 al., 2024; 1.1 – 4: Schroeder et al., 2017) and China 0.6 – 1.5/1.25 – 2.39 (Chen et al., 2023)



912 during the summer season are also compared with our model estimates. The estimated FNR  
913 values from the ECHAM6–HAMOZ simulations show fair agreement over both locations (0.4  
914 – 4.6 in the US and 0.58 – 2.56 in China) with some minor differences. These minor  
915 discrepancies in the estimated FNR could be due to differences in the chosen location, time  
916 period and dataset used. Chen et al. (2023) have also reported that the transition limits depend  
917 on the region considered for the analysis.

918

919 Based on the threshold values depicted in Table 4 and the mean FNR in Figure 12, the seasonal  
920 change in ozone photochemical regimes over the key regions associated with the different  
921 emission scenarios are assessed. In the CTL simulation (Fig. 12e – h), the US, Europe, and  
922 China are found to be in the transition regime, while all other regions are NO<sub>x</sub>–limited during  
923 winter. In spring every region except India remains NO<sub>x</sub>–limited, with India transitioning into  
924 the transition regime. During summer and autumn, all regions shift to a NO<sub>x</sub>–limited condition.  
925 We further compared the model-estimated regional FNR from the CTL simulation with the  
926 OMI-derived FNR shown in Figure 12a – d. The ozone photochemical regimes inferred from  
927 both OMI and the model show consistent results except during winter. During winter, the US,  
928 Europe and China are NO<sub>x</sub> limited in OMI, while our model shows them in the transition  
929 regimes.

930

931 Doubling NO<sub>x</sub> (DNO<sub>x</sub>) leads to a shift to a VOC–limited regime in all regions except Africa  
932 and Australia during winter, spring, and autumn (Fig 12i – l). The relatively high VOC  
933 contributions in Africa and Australia likely keep these regions in the transition regime. During  
934 summer, the US, Europe, Africa and Australia transform to the transition regimes, while all  
935 other regions remain VOC–limited. In both the DVOC and HNO<sub>x</sub> scenarios (Fig 12m – t),  
936 ozone photochemical regimes show no seasonality. All regions consistently exhibit a NO<sub>x</sub>–  
937 limited regime throughout all seasons. In the HVOC simulation (Figure 12u – x), the US,  
938 Europe, and China are in transition regimes, while all other regions become NO<sub>x</sub>–limited  
939 during winter. India remains in a transition regime during all other seasons, whereas other  
940 regions consistently exhibit NO<sub>x</sub>–limited conditions.

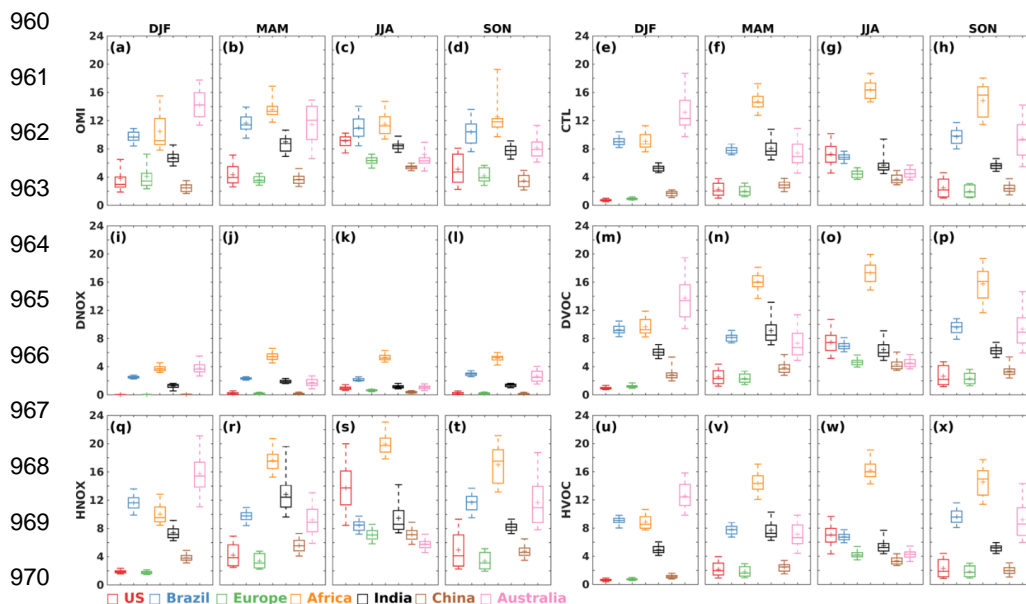
941

942



943 Table 4. Seasonal mean estimated values of the tropospheric HCHO/NO<sub>2</sub> columns threshold  
 944 ratios from ECHAM6–HAMMOZ model control simulation to identify the NO<sub>x</sub> and VOC  
 945 sensitive regimes across regions mentioned in Figure 9. The FNR less than the lower limit  
 946 indicates VOC–limited, and that higher than the upper limit indicates NO<sub>x</sub>–limited regimes.

Sr. No.	Regions	Transition limits of FNR							
		DJF		MAM		JJA		SON	
1	US	0.48	1.04	0.49	1.15	0.49	4.69	0.45	1.39
2	Brazil	2.93	7.79	2.93	6.66	2.93	6.02	3.12	8.44
3	European Union	0.33	1.13	0.33	1.17	0.33	3.32	0.3	1.45
4	Central Africa	2.95	7.26	2.92	5.66	2.93	6.56	3.14	7.06
5	India	2.23	3.91	2.22	9.19	2.22	5.76	2.27	5.29
6	China	0.56	1.85	0.57	1.86	0.58	2.56	1.14	2.01
7	South Australia	1.1	5.54	1.09	2.3	1.09	1.82	1.12	3.93



971 Figure 12. Box and whisker plot illustrating the long-term seasonal average FNR over the  
 972 regions depicted in Fig.7. Box represents 25 and 75 percentile and whisker represents 5 and 95  
 973 percentiles. The plus marker represents the mean, and the horizontal bar represents the 1 and  
 974 99 percentiles.





975 **6. Influence of NO<sub>x</sub> and VOCs emissions on trends of Formaldehyde to Nitrogen dioxide**  
976 **Ratio**

977

978 Trend analysis is carried out on FNR to understand the temporal evolution of ozone  
979 photochemical regimes associated with different emission scenarios. Figure 13 illustrates  
980 trends of FNR during the period 1998 – 2019 from CTL, DNO<sub>x</sub>, DVOC, HNO<sub>x</sub>, and HVOC  
981 simulations. In CTL simulation, decreasing (negative) trends in FNR are seen over the Asian  
982 region (-0.4 to -1.2 decade<sup>-1</sup>) and Australia (-0.8 to -1.6 decade<sup>-1</sup>), and an increasing (positive)  
983 trend in Europe (0.2 decade<sup>-1</sup>) and the US (0.8 – 1.4 decade<sup>-1</sup>) (Fig. 13a). These observed  
984 trends in FNR are mainly driven by the region-specific trends in HCHO and NO<sub>2</sub> (Fig. 7).  
985 Figure 7 shows a higher positive trend in NO<sub>2</sub> than in HCHO in the Asia region, causing an  
986 overall decreasing trend in FNR, indicating a tendency towards VOC-limited regimes.  
987 Whereas, over the US and Europe, there is a higher negative trend in NO<sub>2</sub> than HCHO, causing  
988 a positive trend in FNR, indicating a tendency towards a NO<sub>x</sub>-limited regime. A recent study  
989 by Elshorbany et al. (2024) also reported a significant positive trend over Europe and the US  
990 and a negative trend over Asia using the OMI-based tropospheric column HCHO/NO<sub>2</sub> ratio.  
991 Further, long-term column measurements of HCHO and NO<sub>2</sub> from OMI over India and China  
992 have revealed an increasing trend in NO<sub>2</sub> compared to that of HCHO, causing a decreasing  
993 trend in FNR over these regions (Jin and Holloway, 2015; Mahajan et al., 2015).

994

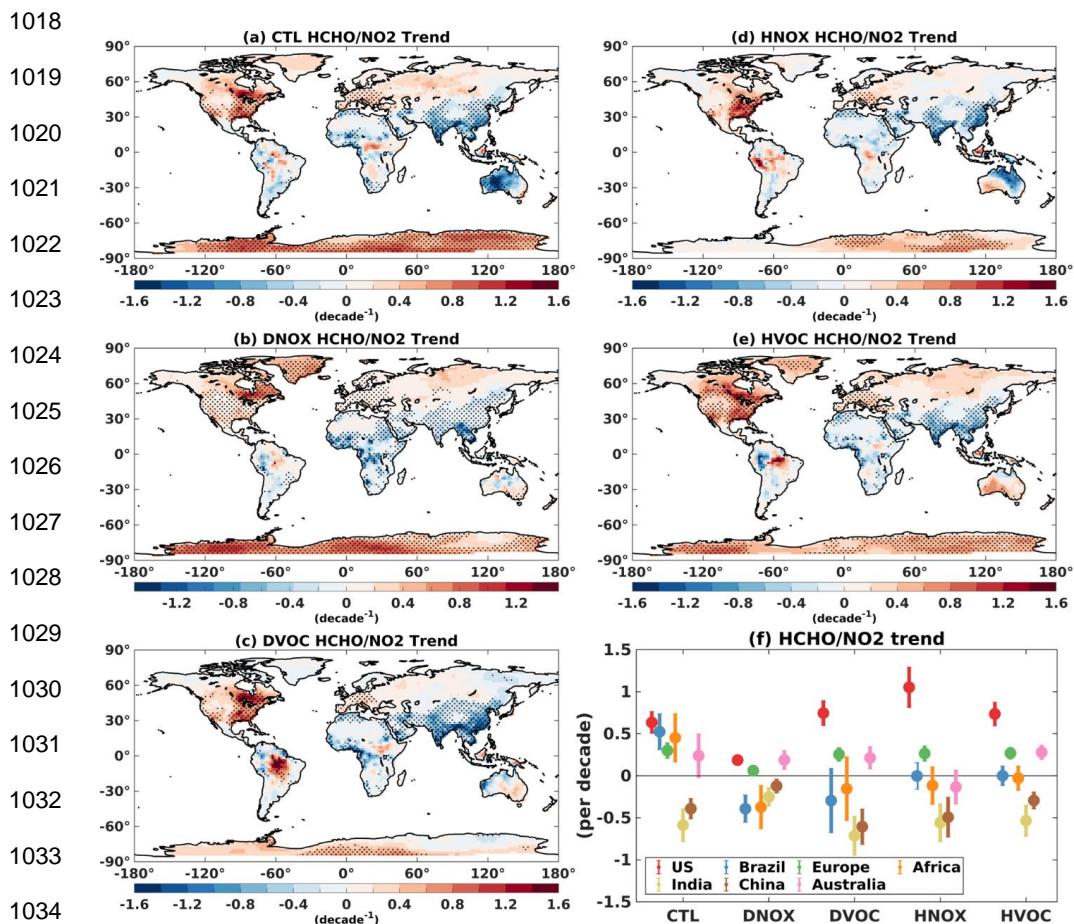
995 DNO<sub>x</sub> simulation (Fig. 13b) shows a similar spatial trend pattern to that of CTL simulation  
996 (Fig. 13a). However, the magnitude of this trend is less than that of the CTL. For example, a  
997 weak positive trend is noted in the US and Europe (0.2 – 0.4 decade<sup>-1</sup>), while trends over India,  
998 and China are less negative (-0.2 to -0.4 decade<sup>-1</sup>) in DNO<sub>x</sub> than CTL. (Fig. 13b). On the  
999 contrary, the magnitude of the positive trend over Canada and the negative trend over central  
1000 Africa increased in DNO<sub>x</sub> emission, while the negative trend over Australia became nominal  
1001 and insignificant. This indicates that Canada and central Africa have a tendency to become  
1002 NO<sub>x</sub>-limited and VOC-limited respectively.

1003 In DVOC simulations, trends are marginally increasing over the US, Canada, and Europe  
1004 compared to the CTL (Fig. 13a and 13c). A notable change is observed over the Middle East  
1005 and Amazon, where trends become more negative and positive respectively compared to CTL.  
1006 The negative trends over Australia in the CTL become nominal and insignificant in the DVOC





1007 simulation. In HNO<sub>x</sub> simulations (Fig. 13d), the positive trends are higher over the US, Europe  
 1008 and Amazon, while negative trends prevail over India, China and northeast Australia.  
 1009 Meanwhile, in HVOC simulation, marginal changes are noted globally compared to CTL. The  
 1010 most pronounced change in the FNR trend is observed over West Australia, where the negative  
 1011 trend in CTL becomes positive in HVOC (Fig. 13e). Figure 13f clearly shows that the trend in  
 1012 FNR is always negative over India and China for all the simulations, indicating that these  
 1013 regions have a tendency to become VOC-limited, while the positive trends over Europe and  
 1014 US show a tendency to become more NO<sub>x</sub>-limited. Further, from Figures 5, 11 and 13, we can  
 1015 infer that the relation between trends in FNR and ozone exhibits a nonlinearity. For example,  
 1016 even though FNR shows a negative trend over India and China for all the simulations, the  
 1017 TRCO trend depends on the specific emission scenario.





1035 Figure 13. Trends in the tropospheric column HCHO/NO<sub>2</sub> ratio during 1998 – 2019 from  
1036 ECHAM6–HAMMOZ simulations for (a) for CTL, (b) DNO<sub>x</sub>, (c) DVOC, (d) HNO<sub>x</sub>, (e)  
1037 HVOC simulations. The stippled region indicates the trend significant at 95% confidence based  
1038 on the t-test. (f) scatter plot illustrating the long-term trend and standard deviation over the  
1039 regions depicted in Fig.9.

1040

## 1041 **7. Tropospheric ozone radiative effects**

1042 The impact of emission changes on the tropospheric ozone radiative effect (TO3RE) is  
1043 estimated using the ECHAM6 model output and a radiative kernel method (see data and model  
1044 experiments). The estimated TO3RE for different model simulations are shown in Figure 14.  
1045 In the CTL simulations (Fig. 14a), the estimated global mean area-weighted average TO3RE  
1046 for the period 1998 to 2019 is 1.21 [1.1 to 1.3] W m<sup>-2</sup>. High TO3RE is noted over North Africa  
1047 and the Middle East region in NH (~2.2 W m<sup>-2</sup>), while in SH, it is over Australia and South  
1048 Africa (~1.2 W m<sup>-2</sup>). TO3RE estimates from TES measurements (2005 – 2009) also show a  
1049 peak of 1.0 W m<sup>-2</sup> in northern Africa, the Mediterranean, and the Middle East in June–July–  
1050 August (Bowman et al. 2013). Recently, Pope et al. (2024) reported TO3RE estimates from  
1051 IASI–SOFID, IASI–FORLI, and IASI–IMS for the period 2008 – 2017. The values reported  
1052 by Pope et al. (2024) are comparable with our CTL simulation (e.g. IASI–FORLI: 1.23 W m<sup>-2</sup>,  
1053 IASI–SOFRID: 1.21 W m<sup>-2</sup>, IASI–IMS: 1.21 W m<sup>-2</sup>). The minor differences in the estimated  
1054 global mean TO3RE from the model and satellites are due to different time periods of  
1055 observations/simulations.

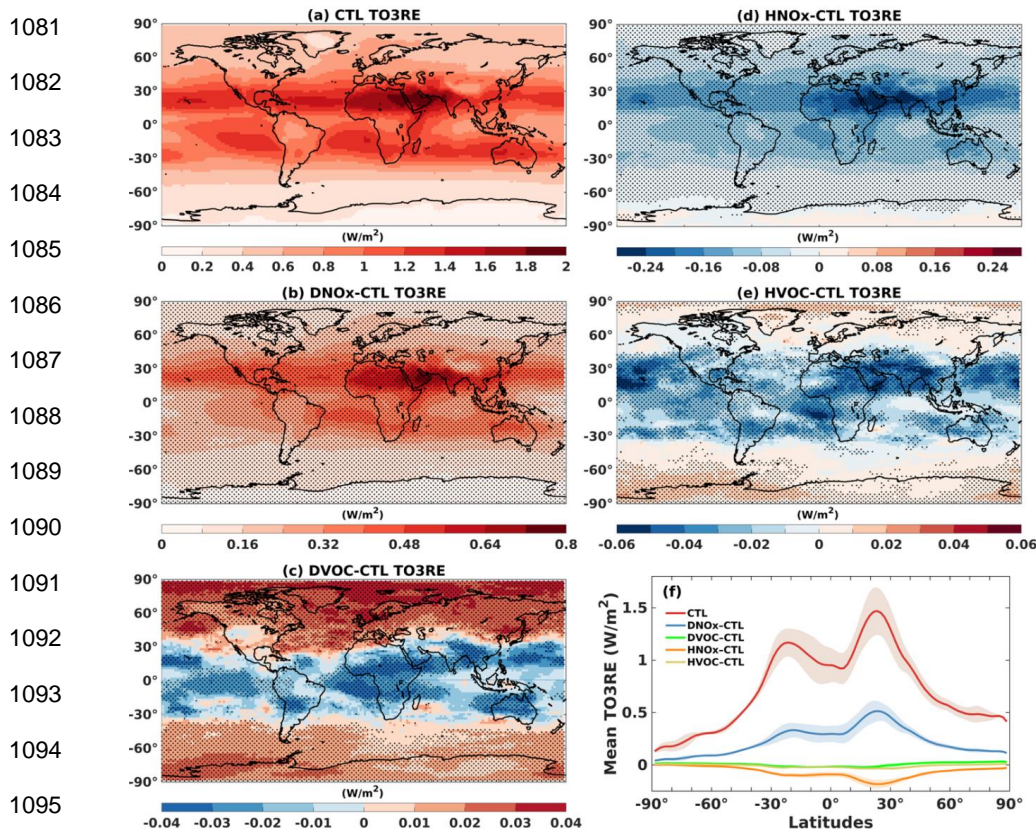
1056

1057 The anomalies of TO3RE from DNO<sub>x</sub>-CTL simulations are shown in Figure 14b. Doubling of  
1058 NO<sub>x</sub> emission causes an enhancement in TO3RE by 0.36 [0.23 to 0.5] W m<sup>-2</sup> compared to the  
1059 CTL simulation. It shows a peak over the Middle East and adjacent North Africa (0.7 W m<sup>-2</sup>).  
1060 A similar peak over this region is also seen in the CTL simulation. Doubling of VOC emissions  
1061 causes a marginal decrease in global mean TO3RE by -0.005 [-0.05 to 0.04] W m<sup>-2</sup>. TRCO  
1062 enhancement for doubling NO<sub>x</sub> is also higher than doubling VOC (see Fig.3). DVOC-CTL  
1063 simulations (Fig. 14 c) show a peak over the Arctic (0.02 W m<sup>-2</sup>). The TO3RE anomalies are  
1064 negative between 30° N – 30° S. These negative anomalies in TO3RE between 30° S – 30° N  
1065 (Fig. 14c) can be attributed to negative anomalies of TRCO (Fig. 3h).

1066 The reduction of NO<sub>x</sub> emission by 50% reduced global mean TO3RE by -0.12 [-0.2 to -0.05]  
1067 W m<sup>-2</sup> than CTL. The anomalies in TO3RE from HNO<sub>x</sub>-CTL simulations (Fig. 14d) show



1068 negative anomalies all over the globe, with a strong decrease over the Middle East and adjacent  
 1069 North Africa ( $-0.25 \text{ W m}^{-2}$ ). Figures 14b and 14d show that the effect of  
 1070 enhancement/reduction of NO<sub>x</sub> emission is high over the Middle East and adjacent North  
 1071 Africa. The reduction of VOC emission by 50% reduced global mean TO<sub>3</sub>RE by  $-0.03$  [ $-0.07$   
 1072 to  $0.02$ ]  $\text{W m}^{-2}$  than CTL simulations (Fig. 14e). HVOC - CTL simulations show negative  
 1073 anomalies of TO<sub>3</sub>RE between  $40^\circ \text{ S} - 40^\circ \text{ N}$  and positive  $0.015 \text{ W m}^{-2}$  (low confidence) over  
 1074 mid-high latitudes in NH and SH. From Figure 14, it is interesting to note that the magnitude  
 1075 of TO<sub>3</sub>RE and its response to emission change is pronounced over the Middle East compared  
 1076 to all other regions. Further, Figure 14f depicts the latitude variation of zonal mean TO<sub>3</sub>RE for  
 1077 different sensitivity simulations. It is clear from Figure 14f that the TO<sub>3</sub>RE response to  
 1078 emission change is large at the northern and southern mid-latitudes, around  $\pm 30^\circ$ . Also, Figure  
 1079 14f clearly indicates that the impacts of NO<sub>x</sub> emission changes are larger than VOCs  
 1080 throughout the latitude band.





1096 Figure 14. Tropospheric Ozone radiative effects (TO3RE) ( $\text{W m}^{-2}$ ) for (a) CTL, and anomalies  
1097 from (b) DNOx - CTL, (c) DVOC - CTL, (d) HNOx - CTL, (e) HVOC - CTL simulations.  
1098 Stippled regions in Figures (b–e) indicate TO3RE significant at 95 % confidence level based  
1099 on the t-test, (f) line plot for zonal mean TO3RE ( $\text{W m}^{-2}$ ) from CTL, DNOx - CTL, DVOC -  
1100 CTL, HNOx - CTL, HVOC - CTL, shades indicate standard deviation.

1101

## 1102 8 Conclusions

1103 In this study, we report variation of tropospheric ozone levels, trends, photochemical regimes  
1104 and radiative effects using the state-of-the-art ECHAM6–HAMMOZ chemistry-climate model  
1105 simulations from 1998 to 2019. The model simulations are validated against multiple satellite  
1106 observations. Our analysis shows that

- 1107 1. The estimated global mean trend in TRCO from CTL simulations for the period 1998 –  
1108 2019 is  $0.89 [-0.07 \text{ to } 2.1] \text{ ppb decade}^{-1}$ . Trend estimates from OMI/MLS ( $1.43 [-0.5 \text{ to } 3.2] \text{ ppb decade}^{-1}$ ) for the period January 2005 to December 2019 show good agreement  
1109 with CTL ( $1.58 [0.3 \text{ to } 3.3] \text{ ppb decade}^{-1}$ ) for the same period.  
1110
- 1111 2. TRCO anomalies from DNOx - CTL simulations show positive trends over Europe, the  
1112 US, Africa, and South America, with a global mean trend of  $1.2 [-0.1 \text{ to } 2.7] \text{ ppb decade}^{-1}$ .  
1113 However, India and China show decreasing TRCO trend  $-2 \text{ to } -4 \text{ ppb decade}^{-1}$ . Surface  
1114 ozone anomalies over these regions show strong negative trends  $-4.8 \text{ to } -8 \text{ ppb decade}^{-1}$ .
- 1115 3. Global mean TRCO trend anomalies from DNOx - CTL simulation is  $1.2 [-0.1 \text{ to } 2.7] \text{ ppb}$   
1116  $\text{decade}^{-1}$ , while for DVOC - CTL is  $0.5 [-0.03 \text{ to } 1.04] \text{ ppb decade}^{-1}$ . Global mean TRCO  
1117 trend anomalies from HNOx - CTL is  $0.47 [-0.76 \text{ to } 1.3] \text{ ppb decade}^{-1}$  and for HVOC -  
1118 CTL is  $0.37 [-0.35 \text{ to } 1.02] \text{ ppb decade}^{-1}$ .
- 1119 4. The spatial distribution of TRCO anomalies shows that enhancement is nearly 12 times  
1120 higher in DNOx - CTL than in DVOC - CTL simulations. The largest increase in surface  
1121 ozone anomalies from DVOC - CTL is observed over Indo-Gangetic Plains, Eastern China  
1122 and the eastern United States ( $4 - 6 \text{ ppb}$ ), where a decrease in surface ozone anomalies is  
1123 observed in the DNOx - CTL simulation. This decrease (increase) in ozone with an increase  
1124 in NOx (VOC) indicates that these regions are VOC-limited.
- 1125 5. The FNR shows that the transition from VOC-limited to NOx-limited happens suddenly  
1126 in response to changes in the emission of NOx/VOC over the US and China. Whereas this  
1127 transition region shows a wider range in Central Africa. Most polluted cities/industrialized  
1128 areas in the US, Canada, Europe, west Russia, East China, Korea and Japan are identified





- 1129 with a low FNR, indicating VOC limited (FNRs  $<2$ ). Meanwhile, NO<sub>x</sub>-limited regimes  
1130 (largest FNR values  $>5$ ) are primarily found in tropical rainforests, savannas, and arid  
1131 climates.
- 1132 6. The DNO<sub>x</sub> simulation shows a notable change in the spatial extent of VOC-limited  
1133 regimes, particularly in the NH. While the SH exhibits minimal change in the spatial extent  
1134 of VOC-limited regimes.
- 1135 7. DVOC simulations reveal persistent VOC-limited regimes over Western Europe, with  
1136 moderate FNR values indicating a transition to NO<sub>x</sub>-limited regimes across most of the  
1137 NH. Comparing CTL and HNO<sub>x</sub> simulations globally shows a shift from VOC to NO<sub>x</sub>-  
1138 limited regimes.
- 1139 8. Comparison of all the emission simulations, DNO<sub>x</sub> and HNO<sub>x</sub> simulations influence the  
1140 shift in tropospheric ozone photochemical regimes compared to DVOC and HVOC  
1141 simulations, highlighting the global sensitivity of ozone photochemistry to NO<sub>x</sub> emissions  
1142 changes.
- 1143 9. Trends estimated from modelled FNR are negative over India ( $-0.6 \text{ decade}^{-1}$ ) and China ( $-$   
1144  $0.4 \text{ decade}^{-1}$ ) in all the simulations, indicating that these regions have a tendency to become  
1145 VOC-limited, while the positive trends over Europe ( $0.3 \text{ decade}^{-1}$ ), US ( $0.63 \text{ decade}^{-1}$ ), and  
1146 Africa ( $0.45 \text{ decade}^{-1}$ ), indicating a tendency to become more NO<sub>x</sub>-limited.
- 1147 10. The estimated global mean tropospheric ozone radiative effect (TO3RE) is 1.21 [1.1 to  
1148 1.3] W m<sup>-2</sup> which is increased by the doubling of NO<sub>x</sub> emissions (DNO<sub>x</sub> - CTL) by 0.36  
1149 [0.23 to 0.5] W m<sup>-2</sup> and VOCs by  $-0.005$  [ $-0.05$  to  $0.04$ ] W m<sup>-2</sup> (DVOC - CTL). However,  
1150 halving NO<sub>x</sub> (HNO<sub>x</sub> - CTL) emissions shows a reduction in the global mean TO3RE by -  
1151  $0.12$  [ $-0.2$  to  $-0.05$ ] W m<sup>-2</sup> and VOC (HVOC - CTL) by  $-0.03$  [ $-0.07$  to  $0.02$ ] W m<sup>-2</sup>.
- 1152 11. We show that anthropogenic NO<sub>x</sub> emissions have a higher impact on tropospheric ozone  
1153 levels, trends, and radiative effects than VOC emissions globally.  
1154

1155 **Author's contribution:** SF and YE initiated the manuscript. SF made the model simulations.  
1156 VS and SC did the analysis of model simulations. Satellite datasets are provided by JZ, BB,  
1157 EF, IG, ID, MR, IS. All authors contributed to the writing of the manuscript.

1158

1159 **Competing interests:** At least one of the (co-)authors is a member of the editorial board of  
1160 Atmospheric Chemistry and Physics.



1161

1162 **Acknowledgements**

1163 S.F. acknowledge the high-performance computing at the Indian Institute of Tropical  
1164 Meteorology Pune, India for supporting the model simulations. RJP was funded by the UK  
1165 Natural Environment Research Council (NERC) by providing funding for the National Centre  
1166 for Earth Observation (NCEO, award reference NE/R016518/1) and funding from the  
1167 European Space Agency (ESA) Climate Change Initiative (CCI) post-doctoral fellowship  
1168 scheme (award reference 4000137140).

1169 **Data availability**

1170 Available from the TOAR FTP server (<ftp://toar@ftpshare.al.noaa.gov>).

1171 **Code availability**

1172 Available from the corresponding author upon reasonable request.

1173 **References:**

1174 Adame, J. A., Gutierrez-Alvarez, I., Cristofanelli, P., Notario, A., Bogeat, J. A., Bolivar, J. P.,  
1175 and Yela, M.: Surface ozone trends at El Arenosillo observatory from a new perspective,  
1176 *Environmental Research*, 214, 113887, <https://doi.org/10.1016/j.envres.2022.113887>, 2022.

1177 Alvarado, L. M. A., Richter, A., Vrekoussis, M., Hilboll, A., Kalisz Hedegaard, A. B.,  
1178 Schneising, O., and Burrows, J. P.: Unexpected long-range transport of glyoxal and  
1179 formaldehyde observed from the Copernicus Sentinel-5 Precursor satellite during the 2018  
1180 Canadian wildfires, *Atmos. Chem. Phys.*, 20, 2057-2072, 10.5194/acp-20-2057-2020, 2020.

1181 Anderson, D. C., Nicely, J. M., Wolfe, G. M., Hanisco, T. F., Salawitch, R. J., Canty, T. P.,  
1182 Dickerson, R. R., Apel, E. C., Baidar, S., Bannan, T. J., Blake, N. J., Chen, D., Dix, B.,  
1183 Fernandez, R. P., Hall, S. R., Hornbrook, R. S., Gregory Huey, L., Josse, B., Jöckel, P.,  
1184 Kinnison, D. E., Koenig, T. K., Le Breton, M., Marécal, V., Morgenstern, O., Oman, L. D.,  
1185 Pan, L. L., Percival, C., Plummer, D., Revell, L. E., Rozanov, E., Saiz-Lopez, A., Stenke, A.,  
1186 Sudo, K., Tilmes, S., Ullmann, K., Volkamer, R., Weinheimer, A. J., and Zeng, G.:  
1187 Formaldehyde in the Tropical Western Pacific: Chemical Sources and Sinks, Convective  
1188 Transport, and Representation in CAM-Chem and the CCM1 Models, *Journal of Geophysical  
1189 Research: Atmospheres*, 122, 11,201-211,226, <https://doi.org/10.1002/2016JD026121>, 2017.

1190 Anglou, I., Glissenaar, I. A., Boersma, K. F., & Eskes, H. (2024). ESA CCI+ OMI L3 monthly  
1191 mean NO2 columns [Data set]. Royal Netherlands Meteorological Institute (KNMI).  
1192 <https://doi.org/10.21944/cci-no2-omi-l3>

1193 Archibald, A. T., Neu, J. L., Elshorbany, Y. F., Cooper, O. R., Young, P. J., Akiyoshi, H., Cox,  
1194 R. A., Coyle, M., Derwent, R. G., Deushi, M., Finco, A., Frost, G. J., Galbally, I. E., Gerosa,  
1195 G., Granier, C., Griffiths, P. T., Hossaini, R., Hu, L., Jöckel, P., Josse, B., Lin, M. Y., Mertens,  
1196 M., Morgenstern, O., Naja, M., Naik, V., Oltmans, S., Plummer, D. A., Revell, L. E., Saiz-  
1197 Lopez, A., Saxena, P., Shin, Y. M., Shahid, I., Shallcross, D., Tilmes, S., Trickl, T., Wallington,  
1198 T. J., Wang, T., Worden, H. M., and Zeng, G.: Tropospheric Ozone Assessment Report: A



- 1199 critical review of changes in the tropospheric ozone burden and budget from 1850 to 2100,  
1200 *Elementa: Science of the Anthropocene*, 8, 10.1525/elementa.2020.034, 2020.
- 1201 Barret, B., Gouzenes, Y., Le Flochmoen, E., and Ferrant, S.: Retrieval of Metop-A/IASI N2O  
1202 Profiles and Validation with NDACC FTIR Data, *Atmosphere*, 12, 219, 2021.
- 1203 Barret, B., Le Flochmoen, E., Sauvage, B., Pavelin, E., Matricardi, M., and Cammas, J. P.: The  
1204 detection of post-monsoon tropospheric ozone variability over south Asia using IASI data,  
1205 *Atmos. Chem. Phys.*, 11, 9533-9548, 10.5194/acp-11-9533-2011, 2011.
- 1206 Beig, G. and Singh, V.: Trends in tropical tropospheric column ozone from satellite data and  
1207 MOZART model, *Geophysical Research Letters*, 34, <https://doi.org/10.1029/2007GL030460>,  
1208 2007.
- 1209 Boersma, K. F., Vinken, G. C. M., and Eskes, H. J.: Representativeness errors in comparing  
1210 chemistry transport and chemistry climate models with satellite UV–Vis tropospheric column  
1211 retrievals, *Geosci. Model Dev.*, 9, 875-898, 10.5194/gmd-9-875-2016, 2016.
- 1212 Borbas, E. and Ruston, B.: The RTTOV UWiremis IR land surface emissivity module, Mission  
1213 Report EUMETSAT NWPSAF-MO-VS-042. [http://nwpsaf.eu/vs\\_reports/nwpsaf-mo-vs-](http://nwpsaf.eu/vs_reports/nwpsaf-mo-vs-042.pdf)  
1214 [042.pdf](http://nwpsaf.eu/vs_reports/nwpsaf-mo-vs-042.pdf), 2010.
- 1215 Chang, C.-Y., Faust, E., Hou, X., Lee, P., Kim, H. C., Hedquist, B. C., and Liao, K.-J.:  
1216 Investigating ambient ozone formation regimes in neighboring cities of shale plays in the  
1217 Northeast United States using photochemical modeling and satellite retrievals, *Atmospheric  
1218 Environment*, 142, 152-170, <https://doi.org/10.1016/j.atmosenv.2016.06.058>, 2016.
- 1219 Chang, K.-L., Cooper, O. R., Gaudel, A., Allaart, M., Ancellet, G., Clark, H., Godin-  
1220 Beekmann, S., Leblanc, T., Van Malderen, R., Nédélec, P., Petropavlovskikh, I., Steinbrecht,  
1221 W., Stübi, R., Tarasick, D. W., and Torres, C.: Impact of the COVID-19 Economic Downturn  
1222 on Tropospheric Ozone Trends: An Uncertainty Weighted Data Synthesis for Quantifying  
1223 Regional Anomalies Above Western North America and Europe, *AGU Advances*, 3,  
1224 e2021AV000542, <https://doi.org/10.1029/2021AV000542>, 2022.
- 1225 Chang, K.-L., Cooper, O. R., Rodriguez, G., Iraci, L. T., Yates, E. L., Johnson, M. S., Gaudel,  
1226 A., Jaffe, D. A., Bernays, N., Clark, H., Effertz, P., Leblanc, T., Petropavlovskikh, I., Sauvage,  
1227 B., and Tarasick, D. W.: Diverging Ozone Trends Above Western North America: Boundary  
1228 Layer Decreases Versus Free Tropospheric Increases, *Journal of Geophysical Research:  
1229 Atmospheres*, 128, e2022JD038090, <https://doi.org/10.1029/2022JD038090>, 2023.
- 1230 Chen, Y., Wang, M., Yao, Y., Zeng, C., Zhang, W., Yan, H., Gao, P., Fan, L., and Ye, D.:  
1231 Research on the ozone formation sensitivity indicator of four urban agglomerations of China  
1232 using Ozone Monitoring Instrument (OMI) satellite data and ground-based measurements,  
1233 *Science of The Total Environment*, 869, 161679,  
1234 <https://doi.org/10.1016/j.scitotenv.2023.161679>, 2023.
- 1235 Cohen, Y., Petetin, H., Thouret, V., Marécal, V., Josse, B., Clark, H., Sauvage, B., Fontaine,  
1236 A., Athier, G., Blot, R., Boulanger, D., Cousin, J. M., and Nédélec, P.: Climatology and long-  
1237 term evolution of ozone and carbon monoxide in the upper troposphere–lower stratosphere  
1238 (UTLS) at northern midlatitudes, as seen by IAGOS from 1995 to 2013, *Atmos. Chem. Phys.*,  
1239 18, 5415-5453, 10.5194/acp-18-5415-2018, 2018.



- 1240 Cooper, O. R., Parrish, D. D., Ziemke, J., Balashov, N. V., Cupeiro, M., Galbally, I. E., Gilge,  
1241 S., Horowitz, L., Jensen, N. R., Lamarque, J.-F., Naik, V., Oltmans, S. J., Schwab, J., Shindell,  
1242 D. T., Thompson, A. M., Thouret, V., Wang, Y., and Zbinden, R. M.: Global distribution and  
1243 trends of tropospheric ozone: An observation-based review, *Elementa: Science of the*  
1244 *Anthropocene*, 2, 10.12952/journal.elementa.000029, 2014.
- 1245 Cuesta, J., Kanaya, Y., Takigawa, M., Dufour, G., Eremenko, M., Foret, G., Miyazaki, K., and  
1246 Beekmann, M.: Transboundary ozone pollution across East Asia: daily evolution and  
1247 photochemical production analysed by IASI + GOME2 multispectral satellite observations and  
1248 models, *Atmos. Chem. Phys.*, 18, 9499-9525, 10.5194/acp-18-9499-2018, 2018.
- 1249 Cuesta, J., Costantino, L., Beekmann, M., Siour, G., Menut, L., Bessagnet, B., Landi, T. C.,  
1250 Dufour, G., and Eremenko, M.: Ozone pollution during the COVID-19 lockdown in the spring  
1251 of 2020 over Europe, analysed from satellite observations, in situ measurements, and models,  
1252 *Atmos. Chem. Phys.*, 22, 4471-4489, 10.5194/acp-22-4471-2022, 2022.
- 1253 Cuesta, J., Eremenko, M., Liu, X., Dufour, G., Cai, Z., Höpfner, M., von Clarmann, T., Sellitto,  
1254 P., Foret, G., Gaubert, B., Beekmann, M., Orphal, J., Chance, K., Spurr, R., and Flaud, J. M.:  
1255 Satellite observation of lowermost tropospheric ozone by multispectral synergism of IASI  
1256 thermal infrared and GOME-2 ultraviolet measurements over Europe, *Atmos. Chem. Phys.*,  
1257 13, 9675-9693, 10.5194/acp-13-9675-2013, 2013.
- 1258 De Smedt, I., Stavrou, T., Hendrick, F., Danckaert, T., Vlemmix, T., Pinardi, G., Theys, N.,  
1259 Lerot, C., Gielen, C., Vigouroux, C., Hermans, C., Fayt, C., Veefkind, P., Müller, J. F., and  
1260 Van Roozendaal, M.: Diurnal, seasonal and long-term variations of global formaldehyde  
1261 columns inferred from combined OMI and GOME-2 observations, *Atmos. Chem. Phys.*, 15,  
1262 12519-12545, 10.5194/acp-15-12519-2015, 2015.
- 1263 De Smedt, I., Theys, N., Yu, H., Danckaert, T., Lerot, C., Compernelle, S., Van Roozendaal,  
1264 M., Richter, A., Hilboll, A., Peters, E., Pedernana, M., Loyola, D., Beirle, S., Wagner, T.,  
1265 Eskes, H., van Geffen, J., Boersma, K. F., and Veefkind, P.: Algorithm theoretical baseline for  
1266 formaldehyde retrievals from S5P TROPOMI and from the QA4ECV project, *Atmos. Meas.*  
1267 *Tech.*, 11, 2395-2426, 10.5194/amt-11-2395-2018, 2018.
- 1268 De Smedt, I., Pinardi, G., Vigouroux, C., Compernelle, S., Bais, A., Benavent, N., Boersma,  
1269 F., Chan, K. L., Donner, S., Eichmann, K. U., Hedelt, P., Hendrick, F., Irie, H., Kumar, V.,  
1270 Lambert, J. C., Langerock, B., Lerot, C., Liu, C., Loyola, D., Píters, A., Richter, A., Rivera  
1271 Cárdenas, C., Romahn, F., Ryan, R. G., Sinha, V., Theys, N., Vlietinck, J., Wagner, T., Wang,  
1272 T., Yu, H., and Van Roozendaal, M.: Comparative assessment of TROPOMI and OMI  
1273 formaldehyde observations and validation against MAX-DOAS network column  
1274 measurements, *Atmos. Chem. Phys.*, 21, 12561-12593, 10.5194/acp-21-12561-2021, 2021.
- 1275 Duncan, B. N., Yoshida, Y., Olson, J. R., Sillman, S., Martin, R. V., Lamsal, L., Hu, Y.,  
1276 Pickering, K. E., Retscher, C., Allen, D. J., and Crawford, J. H.: Application of OMI  
1277 observations to a space-based indicator of NO<sub>x</sub> and VOC controls on surface ozone formation,  
1278 *Atmospheric Environment*, 44, 2213-2223, <https://doi.org/10.1016/j.atmosenv.2010.03.010>,  
1279 2010.
- 1280 Edwards, J. M. and Slingo, A.: Studies with a flexible new radiation code. I: Choosing a  
1281 configuration for a large-scale model, *Quarterly Journal of the Royal Meteorological Society*,  
1282 122, 689-719, <https://doi.org/10.1002/qj.49712253107>, 1996.





- 1283 Elshorbany, Y., Ziemke, J., Strode, S., Petetin, H., Miyazaki, K., De Smedt, I., Pickering, K.,  
1284 Seguel, R., Worden, H., Emmerichs, T., Taraborrelli, D., Cazorla, M., Fadnavis, S., Buchholz,  
1285 R., Gaubert, B., Rojas, N., Nogueira, T., Salameh, T., and Huang, M.: Tropospheric Ozone  
1286 Precursors: Global and Regional Distributions, Trends and Variability, *EGUsphere*, 2024, 1-  
1287 57, 10.5194/egusphere-2024-720, 2024.
- 1288 Emmons, L. K., Apel, E. C., Lamarque, J. F., Hess, P. G., Avery, M., Blake, D., Brune, W.,  
1289 Campos, T., Crawford, J., DeCarlo, P. F., Hall, S., Heikes, B., Holloway, J., Jimenez, J. L.,  
1290 Knapp, D. J., Kok, G., Mena-Carrasco, M., Olson, J., O'Sullivan, D., Sachse, G., Walega, J.,  
1291 Weibring, P., Weinheimer, A., and Wiedinmyer, C.: Impact of Mexico City emissions on  
1292 regional air quality from MOZART-4 simulations, *Atmos. Chem. Phys.*, 10, 6195-6212,  
1293 10.5194/acp-10-6195-2010, 2010.
- 1294 EPA, O. U. Air Pollutant Emissions Trends Data. [https://www.epa.gov/air-emissions-](https://www.epa.gov/air-emissions-inventories/air-pollutant-emissions-trends-data)  
1295 [inventories/air-pollutant-emissions-trends-data](https://www.epa.gov/air-emissions-inventories/air-pollutant-emissions-trends-data), 2023
- 1296 Fadnavis, S., Sabin, T. P., Rap, A., Müller, R., Kubin, A., and Heinold, B.: The impact of  
1297 COVID-19 lockdown measures on the Indian summer monsoon, *Environmental Research*  
1298 *Letters*, 16, 074054, 10.1088/1748-9326/ac109c, 2021a.
- 1299 Fadnavis, S., Heinold, B., Sabin, T. P., Kubin, A., Huang, K., Rap, A., and Müller, R.: Air  
1300 pollution reductions caused by the COVID-19 lockdown open up a way to preserve the  
1301 Himalayan glaciers, *Atmos. Chem. Phys.*, 23, 10439-10449, 10.5194/acp-23-10439-2023,  
1302 2023.
- 1303 Fadnavis, S., Sabin, T. P., Roy, C., Rowlinson, M., Rap, A., Vernier, J.-P., and Sioris, C. E.:  
1304 Elevated aerosol layer over South Asia worsens the Indian droughts, *Scientific Reports*, 9,  
1305 10268, 10.1038/s41598-019-46704-9, 2019a.
- 1306 Fadnavis, S., Müller, R., Kalita, G., Rowlinson, M., Rap, A., Li, J. L. F., Gasparini, B., and  
1307 Laakso, A.: The impact of recent changes in Asian anthropogenic emissions of SO<sub>2</sub> on sulfate  
1308 loading in the upper troposphere and lower stratosphere and the associated radiative changes,  
1309 *Atmos. Chem. Phys.*, 19, 9989-10008, 10.5194/acp-19-9989-2019, 2019b.
- 1310 Fadnavis, S., Chavan, P., Joshi, A., Sonbawne, S. M., Acharya, A., Devara, P. C. S., Rap, A.,  
1311 Ploeger, F., and Müller, R.: Tropospheric warming over the northern Indian Ocean caused by  
1312 South Asian anthropogenic aerosols: possible impact on the upper troposphere and lower  
1313 stratosphere, *Atmos. Chem. Phys.*, 22, 7179-7191, 10.5194/acp-22-7179-2022, 2022.
- 1314 Fadnavis, S., Müller, R., Chakraborty, T., Sabin, T. P., Laakso, A., Rap, A., Griessbach, S.,  
1315 Vernier, J.-P., and Tilmes, S.: The role of tropical volcanic eruptions in exacerbating Indian  
1316 droughts, *Scientific Reports*, 11, 2714, 10.1038/s41598-021-81566-0, 2021b.
- 1317 Fiore, A. M., Hancock, S. E., Lamarque, J.-F., Correa, G. P., Chang, K.-L., Ru, M., Cooper,  
1318 O., Gaudel, A., Polvani, L. M., Sauvage, B., and Ziemke, J. R.: Understanding recent  
1319 tropospheric ozone trends in the context of large internal variability: a new perspective from  
1320 chemistry-climate model ensembles, *Environmental Research: Climate*, 1, 025008,  
1321 10.1088/2752-5295/ac9cc2, 2022.
- 1322 Fleming, Z. L., Doherty, R. M., von Schneidmesser, E., Malley, C. S., Cooper, O. R., Pinto,  
1323 J. P., Colette, A., Xu, X., Simpson, D., Schultz, M. G., Lefohn, A. S., Hamad, S., Moolla, R.,  
1324 Solberg, S., and Feng, Z.: Tropospheric Ozone Assessment Report: Present-day ozone



- 1325 distribution and trends relevant to human health, *Elementa: Science of the Anthropocene*, 6,  
1326 10.1525/elementa.273, 2018.
- 1327 Forster, P., Storelvmo, T., Armour, K., Collins, W., Dufresne, J.-L., Frame, D., Lunt, D. J.,  
1328 Mauritsen, T., Palmer, M. D., Watanabe, M., Wild, M., and Zhang, H.: The Earth's Energy  
1329 Budget, Climate Feedbacks and Climate Sensitivity, in: *Climate Change 2021: The Physical  
1330 Science Basis. Contribution of Working Group I to the Sixth Assessment Report of the  
1331 Intergovernmental Panel on Climate Change* [Masson-Delmotte, V., P. Zhai, A. Pirani, S.L.  
1332 Connors, C. Péan, S. Berger, N. Caud, Y. Chen, L. Goldfarb, M.I. Gomis, M. Huang, K.  
1333 Leitzell, E. Lonnoy, J.B.R. Matthews, T.K. Maycock, T. Waterfield, O. Yelekçi, R. Yu, and B.  
1334 Zhou (eds.)], edited by: Intergovernmental Panel on Climate, C., Cambridge University Press,  
1335 Cambridge, 923-1054, DOI: 10.1017/9781009157896.009, 2021.
- 1336 Forster, P. M., Smith, C., Walsh, T., Lamb, W. F., Lamboll, R., Hall, B., Hauser, M., Ribes,  
1337 A., Rosen, D., Gillett, N. P., Palmer, M. D., Rogelj, J., von Schuckmann, K., Trewin, B., Allen,  
1338 M., Andrew, R., Betts, R. A., Borger, A., Boyer, T., Broersma, J. A., Buontempo, C., Burgess,  
1339 S., Cagnazzo, C., Cheng, L., Friedlingstein, P., Gettelman, A., Gütschow, J., Ishii, M., Jenkins,  
1340 S., Lan, X., Morice, C., Mühle, J., Kadow, C., Kennedy, J., Killick, R. E., Krummel, P. B.,  
1341 Minx, J. C., Myhre, G., Naik, V., Peters, G. P., Pirani, A., Pongratz, J., Schleussner, C. F.,  
1342 Seneviratne, S. I., Szopa, S., Thorne, P., Kovilakam, M. V. M., Majamäki, E., Jalkanen, J. P.,  
1343 van Marle, M., Hoesly, R. M., Rohde, R., Schumacher, D., van der Werf, G., Vose, R.,  
1344 Zickfeld, K., Zhang, X., Masson-Delmotte, V., and Zhai, P.: Indicators of Global Climate  
1345 Change 2023: annual update of key indicators of the state of the climate system and human  
1346 influence, *Earth Syst. Sci. Data*, 16, 2625-2658, 10.5194/essd-16-2625-2024, 2024.
- 1347 Gaudel, A., Bourgeois, I., Li, M., Chang, K. L., Ziemke, J., Sauvage, B., Stauffer, R. M.,  
1348 Thompson, A. M., Kollonige, D. E., Smith, N., Hubert, D., Keppens, A., Cuesta, J., Heue, K.  
1349 P., Veeffkind, P., Aikin, K., Peischl, J., Thompson, C. R., Ryerson, T. B., Frost, G. J.,  
1350 McDonald, B. C., and Cooper, O. R.: Tropical tropospheric ozone distribution and trends from  
1351 in situ and satellite data, *EGUsphere*, 2024, 1-51, 10.5194/egusphere-2023-3095, 2024.
- 1352 Gaudel, A., Cooper, O. R., Ancellet, G., Barret, B., Boynard, A., Burrows, J. P., Clerbaux, C.,  
1353 Coheur, P.-F., Cuesta, J., Cuevas, E., Doniki, S., Dufour, G., Ebojje, F., Foret, G., Garcia, O.,  
1354 Granados-Muñoz, M. J., Hannigan, J. W., Hase, F., Hassler, B., Huang, G., Hurtmans, D.,  
1355 Jaffe, D., Jones, N., Kalabokas, P., Kerridge, B., Kulawik, S., Latter, B., Leblanc, T., Le  
1356 Flochmoën, E., Lin, W., Liu, J., Liu, X., Mahieu, E., McClure-Begley, A., Neu, J. L., Osman,  
1357 M., Palm, M., Petetin, H., Petropavlovskikh, I., Querel, R., Rappoe, N., Rozanov, A., Schultz,  
1358 M. G., Schwab, J., Siddans, R., Smale, D., Steinbacher, M., Tanimoto, H., Tarasick, D. W.,  
1359 Thouret, V., Thompson, A. M., Trickl, T., Weatherhead, E., Wespes, C., Worden, H. M.,  
1360 Vigouroux, C., Xu, X., Zeng, G., and Ziemke, J.: Tropospheric Ozone Assessment Report:  
1361 Present-day distribution and trends of tropospheric ozone relevant to climate and global  
1362 atmospheric chemistry model evaluation, *Elementa: Science of the Anthropocene*, 6,  
1363 10.1525/elementa.291, 2018.
- 1364 Glissenaar, I. A., Anglou, I., Boersma, K. F., & Eskes, H. ESA CCI+ TROPOMI L3 monthly  
1365 mean NO<sub>2</sub> columns [Data set]. Royal Netherlands Meteorological Institute (KNMI).  
1366 <https://doi.org/10.21944/CCI-NO2-TROPOMI-L3>, 2024
- 1367 Goldberg, D. L., Anenberg, S. C., Kerr, G. H., Mohegh, A., Lu, Z., and Streets, D. G.:  
1368 TROPOMI NO<sub>2</sub> in the United States: A Detailed Look at the Annual Averages, *Weekly*



- 1369 Cycles, Effects of Temperature, and Correlation With Surface NO<sub>2</sub> Concentrations, Earth's  
1370 Future, 9, e2020EF001665, <https://doi.org/10.1029/2020EF001665>, 2021.
- 1371 Griffiths, P. T., Murray, L. T., Zeng, G., Shin, Y. M., Abraham, N. L., Archibald, A. T., Deushi,  
1372 M., Emmons, L. K., Galbally, I. E., Hassler, B., Horowitz, L. W., Keeble, J., Liu, J., Moeini,  
1373 O., Naik, V., O'Connor, F. M., Oshima, N., Tarasick, D., Tilmes, S., Turnock, S. T., Wild, O.,  
1374 Young, P. J., and Zanis, P.: Tropospheric ozone in CMIP6 simulations, *Atmos. Chem. Phys.*,  
1375 21, 4187-4218, 10.5194/acp-21-4187-2021, 2021.
- 1376 Guan, J., Jin, B., Ding, Y., Wang, W., Li, G., and Ciren, P.: Global Surface HCHO Distribution  
1377 Derived from Satellite Observations with Neural Networks Technique, *Remote Sensing*, 13,  
1378 4055, 2021.
- 1379 Guenther, A. B., Jiang, X., Heald, C. L., Sakulyanontvittaya, T., Duhl, T., Emmons, L. K., and  
1380 Wang, X.: The Model of Emissions of Gases and Aerosols from Nature version 2.1  
1381 (MEGAN2.1): an extended and updated framework for modeling biogenic emissions, *Geosci.*  
1382 *Model Dev.*, 5, 1471-1492, 10.5194/gmd-5-1471-2012, 2012.
- 1383 Gulev, S. K., Thorne, P. W., Ahn, J., Dentener, F. J., Domingues, C. M., Gerland, S., Gong,  
1384 D., Kaufman, D. S., Nnamchi, H. C., Quaas, J., Rivera, J. A., Sathyendranath, S., Smith, S. L.,  
1385 Trewin, B., von Schuckmann, K., and Vose, R. S.: Changing State of the Climate System, in:  
1386 *Climate Change 2021 – The Physical Science Basis: Working Group I Contribution to the Sixth*  
1387 *Assessment Report of the Intergovernmental Panel on Climate Change* [Masson-Delmotte, V.,  
1388 P. Zhai, A. Pirani, S.L. Connors, C. Péan, S. Berger, N. Caud, Y. Chen, L. Goldfarb, M.I.  
1389 Gomis, M. Huang, K. Leitzell, E. Lonnoy, J.B.R. Matthews, T.K. Maycock, T. Waterfield, O.  
1390 Yelekçi, R. Yu, and B. Zhou (eds.)], edited by: Intergovernmental Panel on Climate, C.,  
1391 Cambridge University Press, Cambridge, 287-422, DOI: 10.1017/9781009157896.004, 2021.
- 1392 Henrot, A. J., Stanelle, T., Schröder, S., Siegenthaler, C., Taraborrelli, D., and Schultz, M. G.:  
1393 Implementation of the MEGAN (v2.1) biogenic emission model in the ECHAM6-HAMMOZ  
1394 chemistry climate model, *Geosci. Model Dev.*, 10, 903-926, 10.5194/gmd-10-903-2017, 2017.
- 1395 Hoffmann, L. and Spang, R.: An assessment of tropopause characteristics of the ERA5 and  
1396 ERA-Interim meteorological reanalyses, *Atmos. Chem. Phys.*, 22, 4019–4046,  
1397 <https://doi.org/10.5194/acp-22-4019-2022>, 2022.
- 1398 Jin, X. and Holloway, T.: Spatial and temporal variability of ozone sensitivity over China  
1399 observed from the Ozone Monitoring Instrument, *Journal of Geophysical Research:*  
1400 *Atmospheres*, 120, 7229-7246, <https://doi.org/10.1002/2015JD023250>, 2015.
- 1401 Jin, X., Fiore, A., Boersma, K. F., Smedt, I. D., and Valin, L.: Inferring Changes in  
1402 Summertime Surface Ozone–NO<sub>x</sub>–VOC Chemistry over U.S. Urban Areas from Two Decades  
1403 of Satellite and Ground-Based Observations, *Environmental Science & Technology*, 54, 6518-  
1404 6529, 10.1021/acs.est.9b07785, 2020.
- 1405 Jin, X., Fiore, A. M., Murray, L. T., Valin, L. C., Lamsal, L. N., Duncan, B., Folkert Boersma,  
1406 K., De Smedt, I., Abad, G. G., Chance, K., and Tonnesen, G. S.: Evaluating a Space-Based  
1407 Indicator of Surface Ozone-NO-VOC Sensitivity Over Midlatitude Source Regions and  
1408 Application to Decadal Trends, *Journal of Geophysical Research: Atmospheres*, 122, 10,439-  
1409 410,461, <https://doi.org/10.1002/2017JD026720>, 2017.



- 1410 Johnson, M. S., Philip, S., Meech, S., Kumar, R., Sorek-Hamer, M., Shiga, Y. P., and Jung, J.:  
1411 Insights into the long-term (2005–2021) spatiotemporal evolution of summer ozone production  
1412 sensitivity in the Northern Hemisphere derived with the Ozone Monitoring Instrument (OMI),  
1413 *Atmos. Chem. Phys.*, 24, 10363–10384, 10.5194/acp-24-10363-2024, 2024.
- 1414 Kinnison, D. E., Brasseur, G. P., Walters, S., Garcia, R. R., Marsh, D. R., Sassi, F., Harvey, V.  
1415 L., Randall, C. E., Emmons, L., Lamarque, J. F., Hess, P., Orlando, J. J., Tie, X. X., Randel,  
1416 W., Pan, L. L., Gettelman, A., Granier, C., Diehl, T., Niemeier, U., and Simmons, A. J.:  
1417 Sensitivity of chemical tracers to meteorological parameters in the MOZART-3 chemical  
1418 transport model, *Journal of Geophysical Research: Atmospheres*, 112,  
1419 <https://doi.org/10.1029/2006JD007879>, 2007.
- 1420 Kleinman, L. I.: Low and high NO<sub>x</sub> tropospheric photochemistry, *Journal of Geophysical*  
1421 *Research: Atmospheres*, 99, 16831–16838, <https://doi.org/10.1029/94JD01028>, 1994.
- 1422 Kumar, V., Beirle, S., Dörner, S., Mishra, A. K., Donner, S., Wang, Y., Sinha, V., and Wagner,  
1423 T.: Long-term MAX-DOAS measurements of NO<sub>2</sub>, HCHO, and aerosols and evaluation of  
1424 corresponding satellite data products over Mohali in the Indo-Gangetic Plain, *Atmos. Chem.*  
1425 *Phys.*, 20, 14183–14235, 10.5194/acp-20-14183-2020, 2020.
- 1426 Lamarque, J. F., Emmons, L. K., Hess, P. G., Kinnison, D. E., Tilmes, S., Vitt, F., Heald, C.  
1427 L., Holland, E. A., Lauritzen, P. H., Neu, J., Orlando, J. J., Rasch, P. J., and Tyndall, G. K.:  
1428 CAM-chem: description and evaluation of interactive atmospheric chemistry in the  
1429 Community Earth System Model, *Geosci. Model Dev.*, 5, 369–411, 10.5194/gmd-5-369-2012,  
1430 2012.
- 1431 Lamarque, J. F., Bond, T. C., Eyring, V., Granier, C., Heil, A., Klimont, Z., Lee, D., Liousse,  
1432 C., Mieville, A., Owen, B., Schultz, M. G., Shindell, D., Smith, S. J., Stehfest, E., Van  
1433 Aardenne, J., Cooper, O. R., Kainuma, M., Mahowald, N., McConnell, J. R., Naik, V., Riahi,  
1434 K., and van Vuuren, D. P.: Historical (1850–2000) gridded anthropogenic and biomass burning  
1435 emissions of reactive gases and aerosols: methodology and application, *Atmos. Chem. Phys.*,  
1436 10, 7017–7039, 10.5194/acp-10-7017-2010, 2010.
- 1437 Lamsal, L. N., Krotkov, N. A., Vasilkov, A., Marchenko, S., Qin, W., Yang, E. S., Fasnacht,  
1438 Z., Joiner, J., Choi, S., Haffner, D., Swartz, W. H., Fisher, B., and Bucsela, E.: Ozone  
1439 Monitoring Instrument (OMI) Aura nitrogen dioxide standard product version 4.0 with  
1440 improved surface and cloud treatments, *Atmos. Meas. Tech.*, 14, 455–479, 10.5194/amt-14-  
1441 455-2021, 2021.
- 1442 Lee, H.-J., Chang, L.-S., Jaffe, D. A., Bak, J., Liu, X., Abad, G. G., Jo, H.-Y., Jo, Y.-J., Lee,  
1443 J.-B., Yang, G.-H., Kim, J.-M., and Kim, C.-H.: Satellite-Based Diagnosis and Numerical  
1444 Verification of Ozone Formation Regimes over Nine Megacities in East Asia, *Remote Sensing*,  
1445 14, 1285, 2022.
- 1446 Lefohn, A. S., Malley, C. S., Simon, H., Wells, B., Xu, X., Zhang, L., and Wang, T.: Responses  
1447 of human health and vegetation exposure metrics to changes in ozone concentration  
1448 distributions in the European Union, United States, and China, *Atmospheric Environment*, 152,  
1449 123–145, <https://doi.org/10.1016/j.atmosenv.2016.12.025>, 2017.
- 1450 Li, M., Kurokawa, J., Zhang, Q., Woo, J. H., Morikawa, T., Chatani, S., Lu, Z., Song, Y., Geng,  
1451 G., Hu, H., Kim, J., Cooper, O. R., and McDonald, B. C.: MIXv2: a long-term mosaic emission



- 1452 inventory for Asia (2010–2017), *Atmos. Chem. Phys.*, 24, 3925–3952, 10.5194/acp-24-3925-  
1453 2024, 2024.
- 1454 Li, S., Yang, Y., Wang, H., Li, P., Li, K., Ren, L., Wang, P., Li, B., Mao, Y., and Liao, H.:  
1455 Rapid increase in tropospheric ozone over Southeast Asia attributed to changes in precursor  
1456 emission source regions and sectors, *Atmospheric Environment*, 304, 119776,  
1457 <https://doi.org/10.1016/j.atmosenv.2023.119776>, 2023.
- 1458 Lin, M., Horowitz, L. W., Oltmans, S. J., Fiore, A. M., and Fan, S.: Tropospheric ozone trends  
1459 at Mauna Loa Observatory tied to decadal climate variability, *Nature Geoscience*, 7, 136–143,  
1460 10.1038/ngeo2066, 2014.
- 1461 Liu, J., Strode, S. A., Liang, Q., Oman, L. D., Colarco, P. R., Fleming, E. L., Manyin, M. E.,  
1462 Douglass, A. R., Ziemke, J. R., Lamsal, L. N., and Li, C.: Change in Tropospheric Ozone in  
1463 the Recent Decades and Its Contribution to Global Total Ozone, *Journal of Geophysical  
1464 Research: Atmospheres*, 127, e2022JD037170, <https://doi.org/10.1029/2022JD037170>, 2022.
- 1465 Lu, X., Zhang, L., Liu, X., Gao, M., Zhao, Y., and Shao, J.: Lower tropospheric ozone over  
1466 India and its linkage to the South Asian monsoon, *Atmos. Chem. Phys.*, 18, 3101–3118,  
1467 10.5194/acp-18-3101-2018, 2018.
- 1468 Mahajan, A. S., De Smedt, I., Biswas, M. S., Ghude, S., Fadnavis, S., Roy, C., and van  
1469 Roozendaal, M.: Inter-annual variations in satellite observations of nitrogen dioxide and  
1470 formaldehyde over India, *Atmospheric Environment*, 116, 194–201,  
1471 <https://doi.org/10.1016/j.atmosenv.2015.06.004>, 2015.
- 1472 Martin, R. V., Fiore, A. M., and Van Donkelaar, A.: Space-based diagnosis of surface ozone  
1473 sensitivity to anthropogenic emissions, *Geophysical Research Letters*, 31,  
1474 <https://doi.org/10.1029/2004GL019416>, 2004.
- 1475 Matricardi, M., Chevallier, F., Kelly, G., and Thépaut, J.-N.: An improved general fast radiative  
1476 transfer model for the assimilation of radiance observations, *Quarterly Journal of the Royal  
1477 Meteorological Society*, 130, 153–173, <https://doi.org/10.1256/qj.02.181>, 2004.
- 1478 Millet, D. B., Jacob, D. J., Boersma, K. F., Fu, T.-M., Kurosu, T. P., Chance, K., Heald, C. L.,  
1479 and Guenther, A.: Spatial distribution of isoprene emissions from North America derived from  
1480 formaldehyde column measurements by the OMI satellite sensor, *Journal of Geophysical  
1481 Research: Atmospheres*, 113, <https://doi.org/10.1029/2007JD008950>, 2008.
- 1482 Mills, G., Pleijel, H., Malley, C. S., Sinha, B., Cooper, O. R., Schultz, M. G., Neufeld, H. S.,  
1483 Simpson, D., Sharps, K., Feng, Z., Gerosa, G., Harmens, H., Kobayashi, K., Saxena, P.,  
1484 Paoletti, E., Sinha, V., and Xu, X.: Tropospheric Ozone Assessment Report: Present-day  
1485 tropospheric ozone distribution and trends relevant to vegetation, *Elementa: Science of the  
1486 Anthropocene*, 6, 10.1525/elementa.302, 2018.
- 1487 Monks, P. S., Archibald, A. T., Colette, A., Cooper, O., Coyle, M., Derwent, R., Fowler, D.,  
1488 Granier, C., Law, K. S., Mills, G. E., Stevenson, D. S., Tarasova, O., Thouret, V., von  
1489 Schneidmesser, E., Sommariva, R., Wild, O., and Williams, M. L.: Tropospheric ozone and  
1490 its precursors from the urban to the global scale from air quality to short-lived climate forcer,  
1491 *Atmos. Chem. Phys.*, 15, 8889–8973, 10.5194/acp-15-8889-2015, 2015.
- 1492 Myhre, G., Shindell, D., Bréon, F.-M., Collins, W., Fuglestedt, J., Huang, J., Koch, D.,  
1493 Lamarque, J.-F., Lee, D., Mendoza, B., Nakajima, T., Robock, A., Stephens, G., Takemura, T.,





- 1494 and Zhang, H.: Anthropogenic and Natural Radiative Forcing, in: *Climate Change 2013: The*  
1495 *Physical Science Basis. Contribution of Working Group I to the Fifth Assessment Report of*  
1496 *the Intergovernmental Panel on Climate Change* [Stocker, T.F., D. Qin, G.-K. Plattner, M.  
1497 Tignor, S.K. Allen, J. Boschung, A. Nauels, Y. Xia, V. Bex and P.M. Midgley (eds.)], edited  
1498 by: Intergovernmental Panel on Climate, C., Cambridge University Press, Cambridge, 659-  
1499 740, doi:10.1017/CBO9781107415324.020, 2013.
- 1500 O3 (IASI+GOME2) – IASI portal: [https://iasi.aeris-data.fr/o3\\_iago2/](https://iasi.aeris-data.fr/o3_iago2/), last access: 28 May 2024
- 1501 Okamoto, S., Cuesta, J., Beekmann, M., Dufour, G., Eremenko, M., Miyazaki, K., Boonne, C.,  
1502 Tanimoto, H., and Akimoto, H.: Impact of different sources of precursors on an ozone pollution  
1503 outbreak over Europe analysed with IASI+GOME2 multispectral satellite observations and  
1504 model simulations, *Atmos. Chem. Phys.*, 23, 7399-7423, 10.5194/acp-23-7399-2023, 2023.
- 1505 Pope, R. J., Rap, A., Pimlott, M. A., Barret, B., Le Flochmoen, E., Kerridge, B. J., Siddans, R.,  
1506 Latter, B. G., Ventress, L. J., Boynard, A., Retscher, C., Feng, W., Rigby, R., Dhomse, S. S.,  
1507 Wespes, C., and Chipperfield, M. P.: Quantifying the tropospheric ozone radiative effect and  
1508 its temporal evolution in the satellite era, *Atmos. Chem. Phys.*, 24, 3613-3626, 10.5194/acp-  
1509 24-3613-2024, 2024.
- 1510 Prather, M., and Zhu X., Lifetimes and timescales of tropospheric ozone, *Lifetimes and*  
1511 *timescales of tropospheric ozone. Elem*, 12, 1, 2024, doi:10.1525/elementa.2023.00112.
- 1512 Putero, D., Cristofanelli, P., Chang, K. L., Dufour, G., Beachley, G., Couret, C., Effertz, P.,  
1513 Jaffe, D. A., Kubistin, D., Lynch, J., Petropavlovskikh, I., Puchalski, M., Sharac, T., Sive, B.  
1514 C., Steinbacher, M., Torres, C., and Cooper, O. R.: Fingerprints of the COVID-19 economic  
1515 downturn and recovery on ozone anomalies at high-elevation sites in North America and  
1516 western Europe, *Atmos. Chem. Phys.*, 23, 15693-15709, 10.5194/acp-23-15693-2023, 2023.
- 1517 Rap, A., Richards, N. A. D., Forster, P. M., Monks, S. A., Arnold, S. R., and Chipperfield, M.  
1518 P.: Satellite constraint on the tropospheric ozone radiative effect, *Geophysical Research*  
1519 *Letters*, 42, 5074-5081, <https://doi.org/10.1002/2015GL064037>, 2015.
- 1520 Rast, S., Schultz, M. G., Bey, I., van Noije, T., Aghedo, A. M., Brasseur, G. P., Diehl, T., Esch,  
1521 M., Ganzeveld, L., Kirchner, I., Kornblueh, L., Rhodin, A., Roeckner, E., Schmidt, H.,  
1522 Schroder, S., Schulzweida, U., Stier, P., Thomas, K., and Walters, S.: Evaluation of the  
1523 tropospheric chemistry general circulation model ECHAM5–MOZ and its application to the  
1524 analysis of the chemical composition of the troposphere with an emphasis on the late RETRO  
1525 period 1990–2000, *Max-Planck-Institut für Meteorologie, Hamburg* 114, 2014.
- 1526 Reick, C. H., Raddatz, T., Brovkin, V., and Gayler, V.: Representation of natural and  
1527 anthropogenic land cover change in MPI-ESM, *Journal of Advances in Modeling Earth*  
1528 *Systems*, 5, 459-482, <https://doi.org/10.1002/jame.20022>, 2013.
- 1529 Ren, J., Guo, F., and Xie, S.: Diagnosing ozone–NO<sub>x</sub>–VOC sensitivity and revealing causes  
1530 of ozone increases in China based on 2013–2021 satellite retrievals, *Atmos. Chem. Phys.*, 22,  
1531 15035-15047, 10.5194/acp-22-15035-2022, 2022.
- 1532 Riese, M. and Ploeger, F. and Rap, A. and Vogel, B. and Konopka, P. and Dameris, M. and  
1533 Forster, P.: Impact of uncertainties in atmospheric mixing on simulated UTLS composition and  
1534 related radiative effects, *J. Geophys. Res.*, 117, D16305, 10.1029/2012JD017751, 2012



- 1535 Roberts, S. J., Salawitch, R. J., Wolfe, G. M., Marvin, M. R., Canty, T. P., Allen, D. J., Hall-  
1536 Quinlan, D. L., Krask, D. J., and Dickerson, R. R.: Multidecadal trends in ozone chemistry in  
1537 the Baltimore-Washington Region, *Atmospheric Environment*, 285, 119239,  
1538 <https://doi.org/10.1016/j.atmosenv.2022.119239>, 2022.
- 1539 Rosanka, S., Franco, B., Clarisse, L., Coheur, P. F., Pozzer, A., Wahner, A., and Taraborrelli,  
1540 D.: The impact of organic pollutants from Indonesian peatland fires on the tropospheric and  
1541 lower stratospheric composition, *Atmos. Chem. Phys.*, 21, 11257-11288, 10.5194/acp-21-  
1542 11257-2021, 2021.
- 1543 Rothman, L. S., Jacquemart, D., Barbe, A., Chris Benner, D., Birk, M., Brown, L. R., Carleer,  
1544 M. R., Chackerian, C., Chance, K., Coudert, L. H., Dana, V., Devi, V. M., Flaud, J. M.,  
1545 Gamache, R. R., Goldman, A., Hartmann, J. M., Jucks, K. W., Maki, A. G., Mandin, J. Y.,  
1546 Massie, S. T., Orphal, J., Perrin, A., Rinsland, C. P., Smith, M. A. H., Tennyson, J., Tolchenov,  
1547 R. N., Toth, R. A., Vander Auwera, J., Varanasi, P., and Wagner, G.: The HITRAN 2004  
1548 molecular spectroscopic database, *Journal of Quantitative Spectroscopy and Radiative*  
1549 *Transfer*, 96, 139-204, <https://doi.org/10.1016/j.jqsrt.2004.10.008>, 2005.
- 1550 Rowlinson, M. J., Rap, A., Hamilton, D. S., Pope, R. J., Hantson, S., Arnold, S. R., Kaplan, J.  
1551 O., Arneeth, A., Chipperfield, M. P., Forster, P. M., and Nieradzik, L.: Tropospheric ozone  
1552 radiative forcing uncertainty due to pre-industrial fire and biogenic emissions, *Atmos. Chem.*  
1553 *Phys.*, 20, 10937-10951, 10.5194/acp-20-10937-2020, 2020.
- 1554 Saunders, R., Matricardi, M., and Brunel, P.: An improved fast radiative transfer model for  
1555 assimilation of satellite radiance observations, *Quarterly Journal of the Royal Meteorological*  
1556 *Society*, 125, 1407-1425, <https://doi.org/10.1002/qj.1999.49712555615>, 1999.
- 1557 Schroeder, J. R., Crawford, J. H., Fried, A., Walega, J., Weinheimer, A., Wisthaler, A., Müller,  
1558 M., Mikoviny, T., Chen, G., Shook, M., Blake, D. R., and Tonnesen, G. S.: New insights into  
1559 the column CH<sub>2</sub>O/NO<sub>2</sub> ratio as an indicator of near-surface ozone sensitivity, *Journal of*  
1560 *Geophysical Research: Atmospheres*, 122, 8885-8907, <https://doi.org/10.1002/2017JD026781>,  
1561 2017.
- 1562 Schultz, M. G., Stadtler, S., Schröder, S., Taraborrelli, D., Franco, B., Krefting, J., Henrot, A.,  
1563 Ferrachat, S., Lohmann, U., Neubauer, D., Siegenthaler-Le Drian, C., Wahl, S., Kokkola, H.,  
1564 Kühn, T., Rast, S., Schmidt, H., Stier, P., Kinnison, D., Tyndall, G. S., Orlando, J. J., and  
1565 Wespes, C.: The chemistry–climate model ECHAM6.3-HAM2.3-MOZ1.0, *Geosci. Model*  
1566 *Dev.*, 11, 1695-1723, 10.5194/gmd-11-1695-2018, 2018.
- 1567 Schultz, M. G., Schröder, S., Lyapina, O., Cooper, O. R., Galbally, I., Petropavlovskikh, I., von  
1568 Schneidemesser, E., Tanimoto, H., Elshorbany, Y., Naja, M., Seguel, R. J., Dauert, U.,  
1569 Eckhardt, P., Feigenspan, S., Fiebig, M., Hjellbrekke, A.-G., Hong, Y.-D., Kjeld, P. C., Koide,  
1570 H., Lear, G., Tarasick, D., Ueno, M., Wallasch, M., Baumgardner, D., Chuang, M.-T., Gillett,  
1571 R., Lee, M., Molloy, S., Moolla, R., Wang, T., Sharps, K., Adame, J. A., Ancellet, G., Apadula,  
1572 F., Artaxo, P., Barlasina, M. E., Bogucka, M., Bonasoni, P., Chang, L., Colomb, A., Cuevas-  
1573 Agulló, E., Cupeiro, M., Degorska, A., Ding, A., Fröhlich, M., Frolova, M., Gadhavi, H.,  
1574 Gheusi, F., Gilge, S., Gonzalez, M. Y., Gros, V., Hamad, S. H., Helmig, D., Henriques, D.,  
1575 Hermansen, O., Holla, R., Hueber, J., Im, U., Jaffe, D. A., Komala, N., Kubistin, D., Lam, K.-  
1576 S., Laurila, T., Lee, H., Levy, I., Mazzoleni, C., Mazzoleni, L. R., McClure-Begley, A.,  
1577 Mohamad, M., Murovec, M., Navarro-Comas, M., Nicodim, F., Parrish, D., Read, K. A., Reid,  
1578 N., Ries, L., Saxena, P., Schwab, J. J., Scorgie, Y., Senik, I., Simmonds, P., Sinha, V.,





- 1579 Skorokhod, A. I., Spain, G., Spangl, W., Spoor, R., Springston, S. R., Steer, K., Steinbacher,  
1580 M., Suharguniyawan, E., Torre, P., Trickl, T., Weili, L., Weller, R., Xiaobin, X., Xue, L., and  
1581 Zhiqiang, M.: Tropospheric Ozone Assessment Report: Database and metrics data of global  
1582 surface ozone observations, *Elementa: Science of the Anthropocene*, 5, 10.1525/elementa.244,  
1583 2017.
- 1584 Scott, C. E., Monks, S. A., Spracklen, D. V., Arnold, S. R., Forster, P. M., Rap, A., Äijälä, M.,  
1585 Artaxo, P., Carslaw, K. S., Chipperfield, M. P., Ehn, M., Gilardoni, S., Heikkinen, L., Kulmala,  
1586 M., Petäjä, T., Reddington, C. L. S., Rizzo, L. V., Swietlicki, E., Vignati, E., and Wilson, C.:  
1587 Impact on short-lived climate forcers increases projected warming due to deforestation, *Nature*  
1588 *Communications*, 9, 157, 10.1038/s41467-017-02412-4, 2018.
- 1589 Shen, L., Jacob, D. J., Zhu, L., Zhang, Q., Zheng, B., Sulprizio, M. P., Li, K., De Smedt, I.,  
1590 González Abad, G., Cao, H., Fu, T.-M., and Liao, H.: The 2005–2016 Trends of Formaldehyde  
1591 Columns Over China Observed by Satellites: Increasing Anthropogenic Emissions of Volatile  
1592 Organic Compounds and Decreasing Agricultural Fire Emissions, *Geophysical Research*  
1593 *Letters*, 46, 4468–4475, <https://doi.org/10.1029/2019GL082172>, 2019.
- 1594 Sillman, S.: The use of NO<sub>x</sub>, H<sub>2</sub>O<sub>2</sub>, and HNO<sub>3</sub> as indicators for ozone-NO<sub>x</sub>-hydrocarbon  
1595 sensitivity in urban locations, *Journal of Geophysical Research: Atmospheres*, 100, 14175–  
1596 14188, <https://doi.org/10.1029/94JD02953>, 1995.
- 1597 Sillman, S., Logan, J. A., and Wofsy, S. C.: The sensitivity of ozone to nitrogen oxides and  
1598 hydrocarbons in regional ozone episodes, *Journal of Geophysical Research: Atmospheres*, 95,  
1599 1837–1851, <https://doi.org/10.1029/JD095iD02p01837>, 1990.
- 1600 Skeie, R. B., Myhre, G., Hodnebrog, Ø., Cameron-Smith, P. J., Deushi, M., Hegglin, M. I.,  
1601 Horowitz, L. W., Kramer, R. J., Michou, M., Mills, M. J., Olivieri, D. J. L., Connor, F. M. O.,  
1602 Paynter, D., Samset, B. H., Sellar, A., Shindell, D., Takemura, T., Tilmes, S., and Wu, T.:  
1603 Historical total ozone radiative forcing derived from CMIP6 simulations, *npj Climate and*  
1604 *Atmospheric Science*, 3, 32, 10.1038/s41612-020-00131-0, 2020.
- 1605 Sofieva, V. F., Tamminen, J., Kyrölä, E., Mielonen, T., Veefkind, P., Hassler, B., and Bodeker,  
1606 G. E.: A novel tropopause-related climatology of ozone profiles, *Atmos. Chem. Phys.*, 14, 283–  
1607 299, 10.5194/acp-14-283-2014, 2014.
- 1608 Souri, A. H., Choi, Y., Jeon, W., Woo, J.-H., Zhang, Q., and Kurokawa, J.-i.: Remote sensing  
1609 evidence of decadal changes in major tropospheric ozone precursors over East Asia, *Journal of*  
1610 *Geophysical Research - Atmospheres*, 122, 2474–2492,  
1611 <https://doi.org/10.1002/2016JD025663>, 2017.
- 1612 Stadtler, S., Simpson, D., Schröder, S., Taraborrelli, D., Bott, A., and Schultz, M.: Ozone  
1613 impacts of gas–aerosol uptake in global chemistry transport models, *Atmos. Chem. Phys.*, 18,  
1614 3147–3171, 10.5194/acp-18-3147-2018, 2018.
- 1615 Steinbrecht, W., Kubistin, D., Plass-Dülmer, C., Davies, J., Tarasick, D. W., von der Gathen,  
1616 P., Deckelmann, H., Jepsen, N., Kivi, R., Lyall, N., Palm, M., Notholt, J., Kois, B., Oelsner,  
1617 P., Allaart, M., Pitters, A., Gill, M., Van Malderen, R., Delcloo, A. W., Sussmann, R., Mahieu,  
1618 E., Servais, C., Romanens, G., Stübi, R., Ancellet, G., Godin-Beekmann, S., Yamanouchi, S.,  
1619 Strong, K., Johnson, B., Cullis, P., Petropavlovskikh, I., Hannigan, J. W., Hernandez, J.-L.,  
1620 Diaz Rodriguez, A., Nakano, T., Chouza, F., Leblanc, T., Torres, C., Garcia, O., Röhling, A.  
1621 N., Schneider, M., Blumenstock, T., Tully, M., Paton-Walsh, C., Jones, N., Querel, R., Strahan,



- 1622 S., Stauffer, R. M., Thompson, A. M., Inness, A., Engelen, R., Chang, K.-L., and Cooper, O.  
1623 R.: COVID-19 Crisis Reduces Free Tropospheric Ozone Across the Northern Hemisphere,  
1624 Geophysical Research Letters, 48, e2020GL091987, <https://doi.org/10.1029/2020GL091987>,  
1625 2021.
- 1626 Stevens, B., Giorgetta, M., Esch, M., Mauritsen, T., Crueger, T., Rast, S., Salzmann, M.,  
1627 Schmidt, H., Bader, J., Block, K., Brokopf, R., Fast, I., Kinne, S., Kornblueh, L., Lohmann,  
1628 U., Pincus, R., Reichler, T., and Roeckner, E.: Atmospheric component of the MPI-M Earth  
1629 System Model: ECHAM6, Journal of Advances in Modeling Earth Systems, 5, 146-172,  
1630 10.1002/jame.20015, 2013.
- 1631 Stevenson, D. S., Dentener, F. J., Schultz, M. G., Ellingsen, K., van Noije, T. P. C., Wild, O.,  
1632 Zeng, G., Amann, M., Atherton, C. S., Bell, N., Bergmann, D. J., Bey, I., Butler, T., Cofala, J.,  
1633 Collins, W. J., Derwent, R. G., Doherty, R. M., Drevet, J., Eskes, H. J., Fiore, A. M., Gauss,  
1634 M., Hauglustaine, D. A., Horowitz, L. W., Isaksen, I. S. A., Krol, M. C., Lamarque, J. F.,  
1635 Lawrence, M. G., Montanaro, V., Müller, J. F., Pitari, G., Prather, M. J., Pyle, J. A., Rast, S.,  
1636 Rodriguez, J. M., Sanderson, M. G., Savage, N. H., Shindell, D. T., Strahan, S. E., Sudo, K.,  
1637 and Szopa, S.: Multimodel ensemble simulations of present-day and near-future tropospheric  
1638 ozone, Journal of Geophysical Research-Atmospheres, 111, 10.1029/2005JD006338, 2006.
- 1639 Surl, L., Palmer, P. I., and González Abad, G.: Which processes drive observed variations of  
1640 HCHO columns over India?, Atmos. Chem. Phys., 18, 4549-4566, 10.5194/acp-18-4549-2018,  
1641 2018.
- 1642 Szopa, S., Naik, V., Adhikary, B., Artaxo, P., Berntsen, T., Collins, W. D., Fuzzi, S., Gallardo,  
1643 L., Kiendler-Scharr, A., Klimont, Z., Liao, H., Unger, N., and Zanis, P.: Short-lived Climate  
1644 Forcers, in: Climate Change 2021: The Physical Science Basis. Contribution of Working Group  
1645 I to the Sixth Assessment Report of the Intergovernmental Panel on Climate Change [Masson-  
1646 Delmotte, V., P. Zhai, A. Pirani, S.L. Connors, C. Péan, S. Berger, N. Caud, Y. Chen, L.  
1647 Goldfarb, M.I. Gomis, M. Huang, K. Leitzell, E. Lonnoy, J.B.R. Matthews, T.K. Maycock, T.  
1648 Waterfield, O. Yelekçi, R. Yu, and B. Zhou (eds.)], edited by: Intergovernmental Panel on  
1649 Climate, C., Cambridge University Press, Cambridge, 817-922, DOI:  
1650 10.1017/9781009157896.008, 2021.
- 1651 Taraborrelli, D., Cabrera-Perez, D., Bacer, S., Gromov, S., Lelieveld, J., Sander, R., and  
1652 Pozzer, A.: Influence of aromatics on tropospheric gas-phase composition, Atmos. Chem.  
1653 Phys., 21, 2615-2636, 10.5194/acp-21-2615-2021, 2021.
- 1654 Tarasick, D. W., Carey-Smith, T. K., Hocking, W. K., Moeini, O., He, H., Liu, J., Osman, M.  
1655 K., Thompson, A. M., Johnson, B. J., Oltmans, S. J., and Merrill, J. T.: Quantifying  
1656 stratosphere-troposphere transport of ozone using balloon-borne ozonesondes, radar  
1657 windprofilers and trajectory models, Atmospheric Environment, 198, 496-509,  
1658 <https://doi.org/10.1016/j.atmosenv.2018.10.040>, 2019.
- 1659 Van Vuuren, D. P., Edmonds, J., Kainuma, M., Riahi, K., Thomson, A., Hibbard, K., Hurtt, G.  
1660 C., Kram, T., Krey, V., Lamarque, J.-F., Masui, T., Meinshausen, M., Nakicenovic, N., Smith,  
1661 S. J., and Rose, S. K.: The representative concentration pathways: an overview, Climatic  
1662 Change, 109, 5, 10.1007/s10584-011-0148-z, 2011.
- 1663 Veefkind, J. P., Aben, I., McMullan, K., Förster, H., de Vries, J., Otter, G., Claas, J., Eskes, H.  
1664 J., de Haan, J. F., Kleipool, Q., van Weele, M., Hasekamp, O., Hoogeveen, R., Landgraf, J.,  
1665 Snel, R., Tol, P., Ingmann, P., Voors, R., Kruizinga, B., Vink, R., Visser, H., and Levelt, P. F.:



- 1666 TROPOMI on the ESA Sentinel-5 Precursor: A GMES mission for global observations of the  
1667 atmospheric composition for climate, air quality and ozone layer applications, *Remote Sensing*  
1668 of Environment, 120, 70-83, <https://doi.org/10.1016/j.rse.2011.09.027>, 2012.
- 1669 Verstraeten, W. W., Neu, J. L., Williams, J. E., Bowman, K. W., Worden, J. R., and Boersma,  
1670 K. F.: Rapid increases in tropospheric ozone production and export from China, *Nature*  
1671 *Geoscience*, 8, 690-695, 10.1038/ngeo2493, 2015.
- 1672 Vignati, E., Wilson, J., and Stier, P.: M7: An efficient size-resolved aerosol microphysics  
1673 module for large-scale aerosol transport models, *Journal of Geophysical Research*,  
1674 *Atmospheres*, 109, 10.1029/2003JD004485, 2004.
- 1675 Wang, H., Lu, X., Jacob, D. J., Cooper, O. R., Chang, K. L., Li, K., Gao, M., Liu, Y., Sheng,  
1676 B., Wu, K., Wu, T., Zhang, J., Sauvage, B., Nédélec, P., Blot, R., and Fan, S.: Global  
1677 tropospheric ozone trends, attributions, and radiative impacts in 1995–2017: an integrated  
1678 analysis using aircraft (IAGOS) observations, ozonesonde, and multi-decadal chemical model  
1679 simulations, *Atmos. Chem. Phys.*, 22, 13753-13782, 10.5194/acp-22-13753-2022, 2022.
- 1680 Wang, W., van der A, R., Ding, J., van Weele, M., and Cheng, T.: Spatial and temporal changes  
1681 of the ozone sensitivity in China based on satellite and ground-based observations, *Atmos.*  
1682 *Chem. Phys.*, 21, 7253-7269, 10.5194/acp-21-7253-2021, 2021.
- 1683 Wang, Y., Lampel, J., Xie, P., Beirle, S., Li, A., Wu, D., and Wagner, T.: Ground-based MAX-  
1684 DOAS observations of tropospheric aerosols, NO<sub>2</sub>, SO<sub>2</sub> and HCHO in Wuxi, China, from  
1685 2011 to 2014, *Atmos. Chem. Phys.*, 17, 2189-2215, 10.5194/acp-17-2189-2017, 2017.
- 1686 WMO, *Meteorology – A three-dimensional science*, World Meteorological Organisation,  
1687 *Bulletin* 6, (Oct), 134–138, 1957.
- 1688 Young, P. J., Naik, V., Fiore, A. M., Gaudel, A., Guo, J., Lin, M. Y., Neu, J. L., Parrish, D. D.,  
1689 Rieder, H. E., Schnell, J. L., Tilmes, S., Wild, O., Zhang, L., Ziemke, J., Brandt, J., Delcloo,  
1690 A., Doherty, R. M., Geels, C., Hegglin, M. I., Hu, L., Im, U., Kumar, R., Luhar, A., Murray,  
1691 L., Plummer, D., Rodriguez, J., Saiz-Lopez, A., Schultz, M. G., Woodhouse, M. T., and Zeng,  
1692 G.: Tropospheric Ozone Assessment Report: Assessment of global-scale model performance  
1693 for global and regional ozone distributions, variability, and trends, *Elementa: Science of the*  
1694 *Anthropocene*, 6, 10.1525/elementa.265, 2018.
- 1695 Zhang, Y. Q., Cooper, O. R., Gaudel, A., Thompson, A. M., Nédélec, P., Ogino, S. Y., and  
1696 West, J. J.: Tropospheric ozone change from 1980 to 2010 dominated by equatorward  
1697 redistribution of emissions, *Nature Geoscience*, 9, 875–+, 10.1038/NGEO2827, 2016.
- 1698 Ziemke, J. R., Chandra, S., and Bhartia, P. K.: A 25-year data record of atmospheric ozone in  
1699 the Pacific from Total Ozone Mapping Spectrometer (TOMS) cloud slicing: Implications for  
1700 ozone trends in the stratosphere and troposphere, *Journal of Geophysical Research -*  
1701 *Atmospheres*, 110, 10.1029/2004JD005687, 2005.
- 1702 Ziemke, J. R., Chandra, S., Duncan, B. N., Froidevaux, L., Bhartia, P. K., Levelt, P. F., and  
1703 Waters, J. W.: Tropospheric ozone determined from aura OMI and MLS: Evaluation of  
1704 measurements and comparison with the Global Modeling Initiative's Chemical Transport  
1705 Model, *Journal of Geophysical Research - Atmospheres*, 111, 10.1029/2006JD007089, 2006.
- 1706 Ziemke, J. R., Oman, L. D., Strode, S. A., Douglass, A. R., Olsen, M. A., McPeters, R. D.,  
1707 Bhartia, P. K., Froidevaux, L., Labow, G. J., Witte, J. C., Thompson, A. M., Haffner, D. P.,



1708 Kramarova, N. A., Frith, S. M., Huang, L. K., Jaross, G. R., Seftor, C. J., Deland, M. T., and  
1709 Taylor, S. L.: Trends in global tropospheric ozone inferred from a composite record of  
1710 TOMS/OMI/MLS/OMPS satellite measurements and the MERRA-2 GMI simulation, *Atmos.*  
1711 *Chem. Phys.*, 19, 3257-3269, 10.5194/acp-19-3257-2019, 2019.

1712